FINAL REPORT

STUDIES OF AURORAL X-RAY IMAGING FROM HIGH ALTITUDE SPACECRAFT

by

D. L. McKenzie, P. F. Mizera, and C. J. Rice

27 June 1980

Space Sciences Laboratory
THE AEROSPACE CORPORATION
El Segundo, CA 90245

This work was supported by the National Aeronautics and Space Administration under Contract NASW-3338.

ABSTRACT

This report summarizes the results of a study of techniques for imaging the aurora from a high altitude satellite at X-ray wavelengths. X-ray observations allow the straightforward derivation of the primary auroral X-ray spectrum and can be made at all local times, day and night. Five candidate imaging systems are identified: X-ray telescope, multiple pinhole camera, coded aperture, rastered collimator, and imaging collimator. Examples of each are specified, subject to common weight and size limits which allow them to be intercompared. The imaging ability of each system is tested using a wide variety of sample spectra which are based on previous satellite observations. The study shows that the pinhole camera and coded aperture are both good auroral imaging systems. The two collimated detectors are significantly less sensitive than the above two systems. The X-ray telescope provides better image quality than the other systems in almost all cases, but a limitation to energies below about 4 keV prevents this system from providing the spectral data essential to deriving electron spectra, energy input to the atmosphere, and atmospheric densities and conductivities. The orbit selection requires a trade-off between spatial resolution and duty cycle. Both the pinhole camera and the coded aperture are best utilized aboard a pointed satellite in an elliptical orbit with apogee $\gtrsim 5\ R_E$.

CONTENTS

I. INTRODUCTION

This report sets forth the results of a study with the principal aim of specifying one or more feasible techniques for imaging the aurora in the X-ray region of the electromagnetic spectrum, using instrumentation aboard a high altitude ($> 4\ R_E$) polar orbiting satellite. The development of remote sensing techniques, such as those to be discussed below, will allow the scientist to obtain information on the energy spectrum of precipitating electrons, the energy input to the upper atmosphere from the magnetosphere, and ultimately from the solar wind, and such physical properties of the ionosphere as the electron density and the electrical conductivity.

Observations at X-ray energies (roughly 1-100 keV) have several advantages when compared to observations in other regions of the spectrum. X-rays above 1 keV are primarily produced by electron bremsstrahlung in the upper atmosphere. The electrons producing this radiation have energies in the same range as the X-rays. These electrons are responsible for a large fraction of the energy transfer from the magnetosphere to the atmosphere. Observations of the bremsstrahlung spectrum allow the derivation of the electron spectrum by a relatively straightforward procedure. Unlike the case at visible wavelengths, the unfolding of the spectrum does not depend upon knowledge or assumptions about atmospheric chemistry. Our DMSP F2 observations of bremsstrahlung X-rays indicate that measurements to energies above 10 keV are needed to derive the electron spectra, and observations by Imhof and his coworkers demonstrate the occasional occurrence of precipitation events with the emission of a measurable flux of X-rays above 50 keV (e.g. Imhof 1975).

The second major advantage of remote sensing of the aurora at X-ray wavelengths is that it is possible to observe an entire aurora simultaneously or nearly simultaneously, including the sunlit sector. We will show later in this report that, provided observations are restricted to energies above about 2 keV, auroral X-rays will dominate those arising from fluorescence by, or scattering of, solar X-rays in the sunlit Earth's atmosphere (see Rugge, McKenzie and Charles 1979). The restriction to energies above 2 keV is not a serious hindrance, except that it does prevent day sector observations of the strong oxygen and nitrogen K line emission predicted by Luhmann and Blake (1977), which would be important for sensing very soft electron fluxes associated with the cusp.

The principal difficulty encountered in observing the aurora at X-ray wavelengths is a low signal level. A frequent consequence of weak signals (or, in some cases, low signal to noise ratio) is that spatial resolution significantly worse than that available at, say, visible wavelengths must be accepted. Thus it may be desirable to carry a high resolution visible-range imager on the satellite to complement an X-ray imaging spectrometer. Nevertheless, a significant amount of otherwise unobtainable physical information about global processes and properties of the upper atmosphere can be obtained from the X-ray observations alone.

The conclusions of the study of auroral X-ray imaging from high altitude spacecraft are presented in the remainder of this final report. Section II is concerned with defining just what is to be measured. The X-ray spectra and morphology of a wide variety of auroral activity are represented by four representative forms and associated spectra which are used later in the report for candidate instrument evaluation. In addition we present background spectra from the following sources: the diffuse component of cosmic X-rays,

diffuse atmospheric X-rays arising from cosmic ray interactions in the atmosphere, and X-rays from the sunlit Earth arising from atmospheric interactions of solar X-rays. In addition, since proportional counters are used as detectors in most of the candidate imaging systems, we will discuss the irreducible internal background present with such a detector. Section III is a study of five candidate imaging systems: X-ray telescopes, pinhole cameras, coded apertures, rastered collimators, and imaging collimators. For each of these systems a representative instrument is specified, subject to common weight and size limitations so that comparisons may be made. The usefulness of each as an auroral X-ray imager is assessed. Section IV discusses orbit parameters and satellite accommodations for those instruments found to be suitable, and summarizes the conclusions of the study.

II. AURORAL X-RAY AND BACKGROUND SPECTRA

By measuring the X-ray spectrum of the aurora, one can derive the auroral electron spectrum. This knowledge, in turn, allows the calculation of the energy input to the atmosphere by electron precipitation, and atmospheric electron densities and conductivities. The simultaneous determination of the electron spectrum over an entire polar region is only possible by a remote sensing technique. X-ray measurements have an advantage over optical measurements, since the optical emission arises from secondary electrons, and complex chemistry is involved in the atmospheric interactions leading to optical emission. Past satellite experiments have measured localized electron spectra. The DMSP F2 J Package* has obtained electron spectra at the time the X-ray experiment was measuring auroral spectra. The electron data are shown in spectrogram form along with X-ray data and the optical images in Figures II-1 through II-4. The satellite was southbound from the north polar cap when these measurements were made, so the ground track crossed an auroral form before the satellite crossed the associated magnetic field line. This means that there is a small delay between the X-ray spectrum and the corresponding electron spectrum. In addition there is an east-west shift of the field line footprint from the ground track that is small compared to the X-ray instrument field of view.

The work of Mizera et al. (1978) shows that the X-ray spectrum can be derived from the primary electron spectrum and indicates that it may be possible to derive electron spectra from X-ray measurements. The measured X-ray spectrum is subject to experimental errors which may be large for weak spec-

*The J Package consists of two electrostatic analyzers, looking up along the earth radius vector and measuring electrons in the $0.05 < E < 20$ keV interval in 16 channels.

Figure II-1: DMSP auroral data. At the top is a visible image (475 - 750 nm). Below that is an X-ray spectrogram and at the bottom are electron spectrograms from the J Package. Data show widespread diffuse emission.

ORIGINAL PAGE IS
OF POOR QUALITY

Figure II-2: DMSP auroral data used in the study by Mizera et al. (1978). Spectrum 2 in this study was obtained at UT 5538.

DMSP-F2 AURORAE, X-RAYS AND ELECTRONS

October 19, 1977

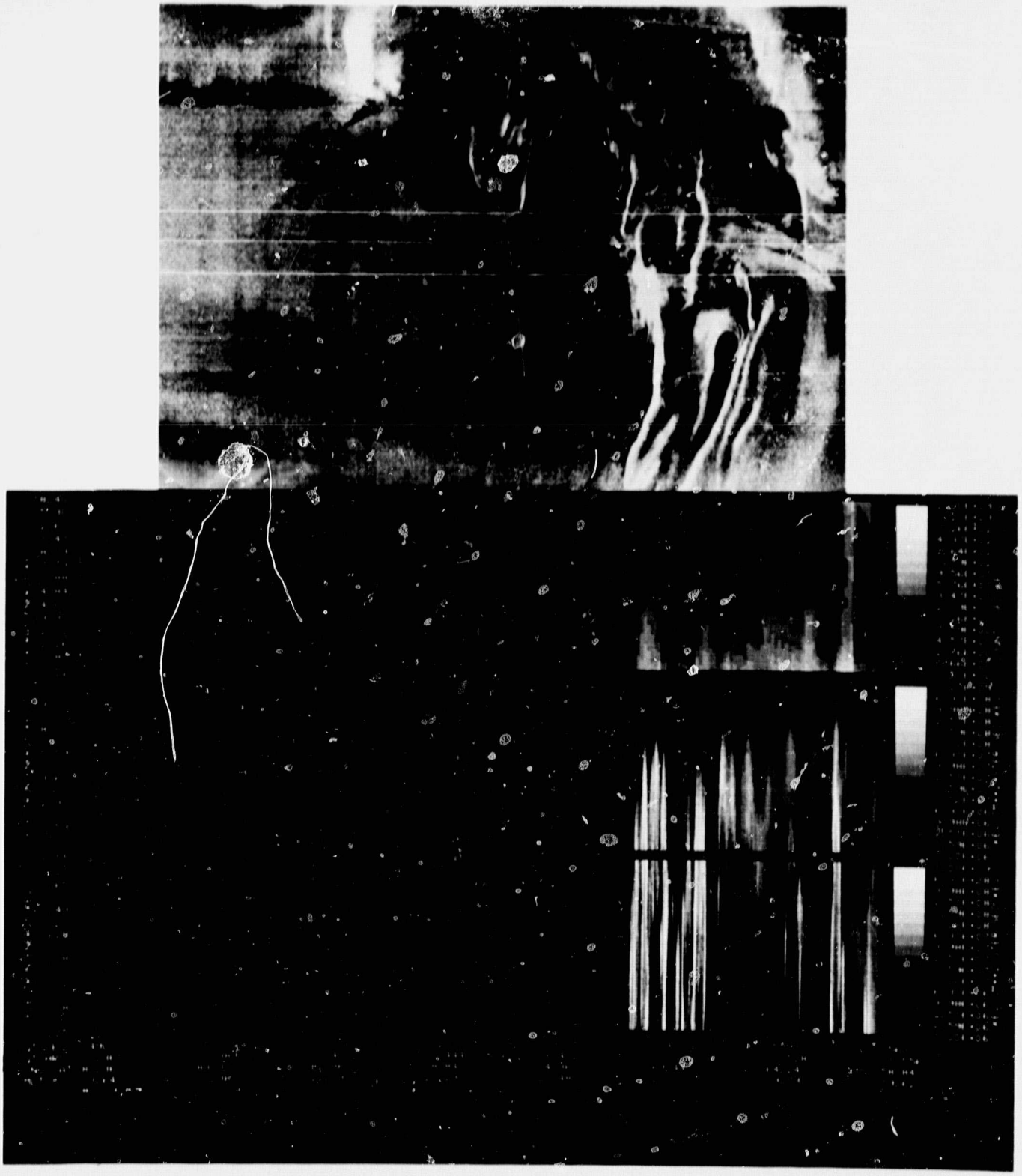

Figure II-3: DMSP auroral data for a westward traveling surge. This is Source 3.

DMSP-F2

NOVEMBER 17, 1977

AURORAL ARCS

X-RAYS

ELECTRONS

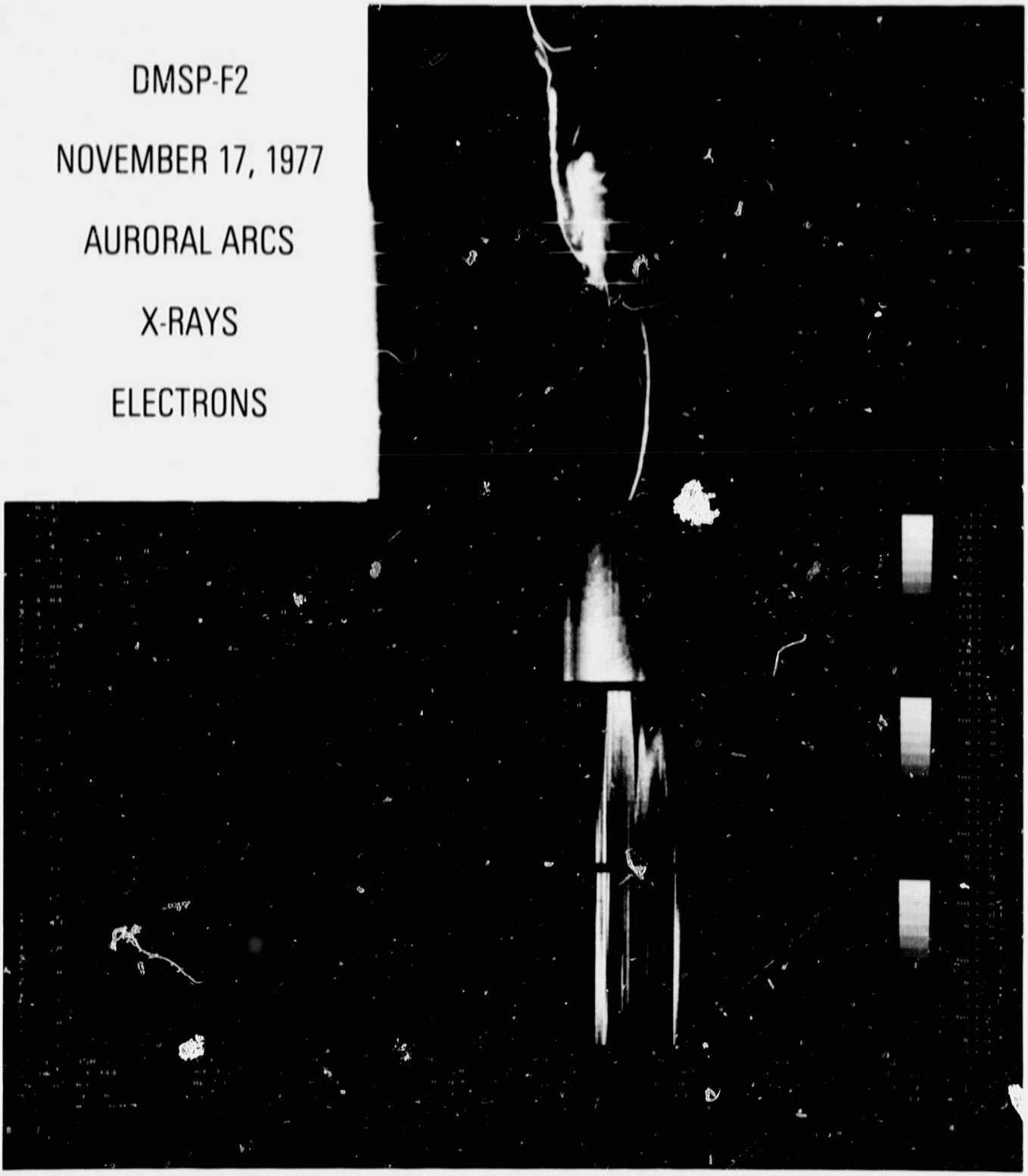

Figure II-4: Auroral arcs observed by DMSP. Source 4 is the bright arc at the right.

DMSP-F2

NOVEMBER 15, 1977

AURORAL ARCS

X-RAYS

ELECTRONS

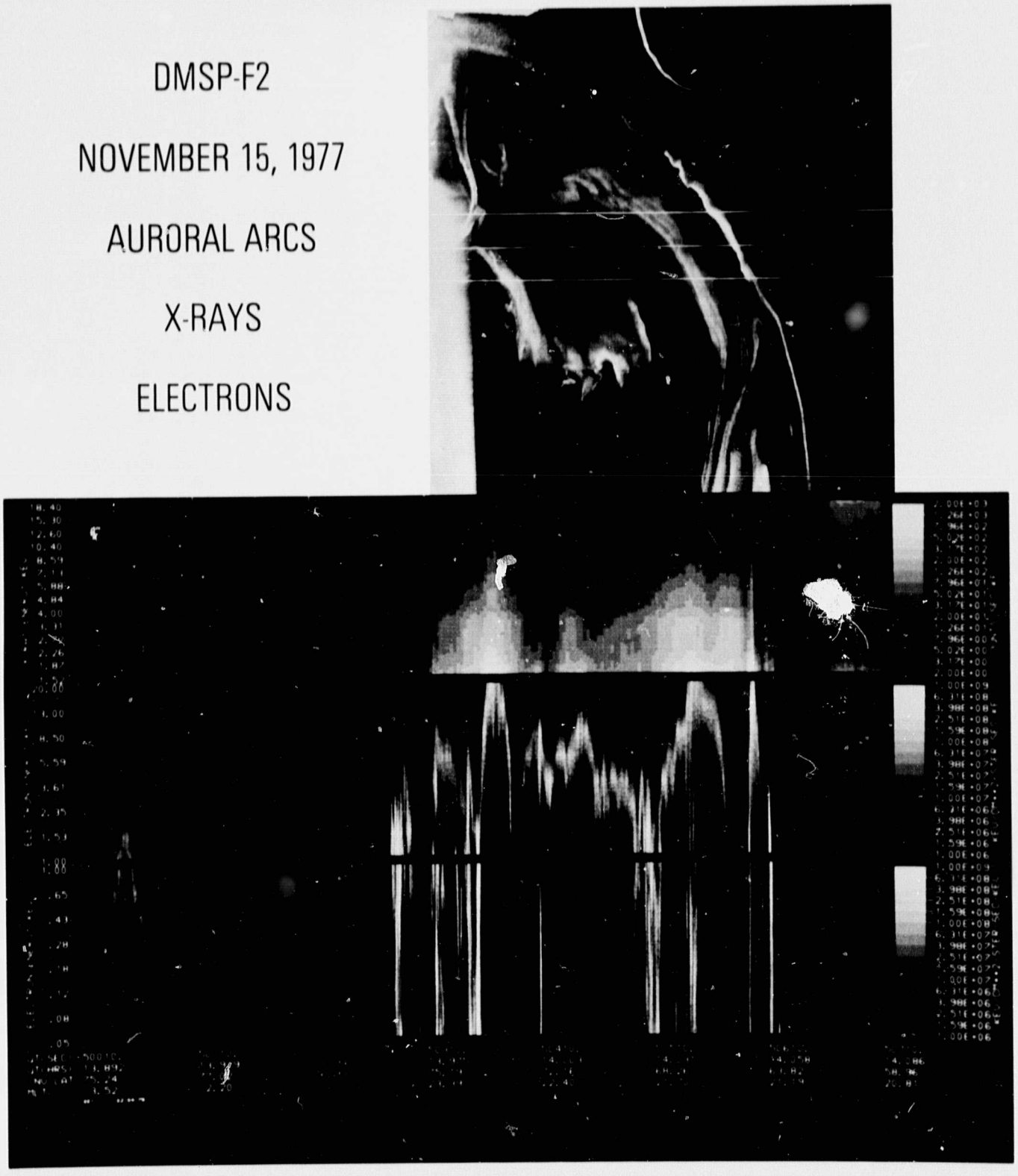

tra. As a result, a given measured X-ray spectrum can arise from a variety of electron spectra. Therefore realistic assumptions must be made regarding the form of the precipitating primary electron spectrum, so that it can be derived from X-ray measurements.

Data derived from past experiments guide the specification of model electron spectra to be fit to the X-ray measurements. Mizera et al. (1978) have analyzed X-ray spectra in Figure II-2 at UT 5373, 5393, 5425, 5446 and 5538 seconds, along with electron spectra at UT 5390, 5405, 5440, 5460 and 5560 seconds. They found that all the electron measurements were approximated well by spectra each consisting of a low energy (1.5 - 3.6 keV) Gaussian of half-width σ (0.75 - 2.0 keV) and a Maxwellian with kT = 3 keV. The X-ray spectra were then calculated from the fitted electron spectra, with no arbitrary normalization factors. The agreement was very good in the last three cases. For the first two cases, the brightest emitting region did not intersect the satellite ground track, which probably explains the observed discrepancy.

The electron spectra discussed by Mizera et al. (1978) have two components. The kT ≈ 3 keV Maxwellian is typical of the distribution in the Earth's plasma sheet. If plasma sheet electrons are accelerated by an electric field parallel to the magnetic field lines, the observed two component spectrum results. The observations discussed above were limited to the energy range between 1.5 keV and about 10 keV. Higher energy X-rays are present in auroral events, and their spectra may be approximated as exponential. The electron spectrum in a given auroral event may then take the form,

$$J(T) = \frac{A}{\sqrt{2\pi}\,\sigma} \exp\left[-(T-T_0)^2/2\sigma^2\right] + BT \exp(-T/3) + C\, e^{-T/\alpha} \quad . \qquad (1)$$

Figure II-5: X-ray spectra from the spectrum "library" fitted to the westward traveling surge spectrum shown in the spectrogram of Figure II-3. At the right the electron spectrum computed from X-ray observations is compared to the measured electron spectrum.

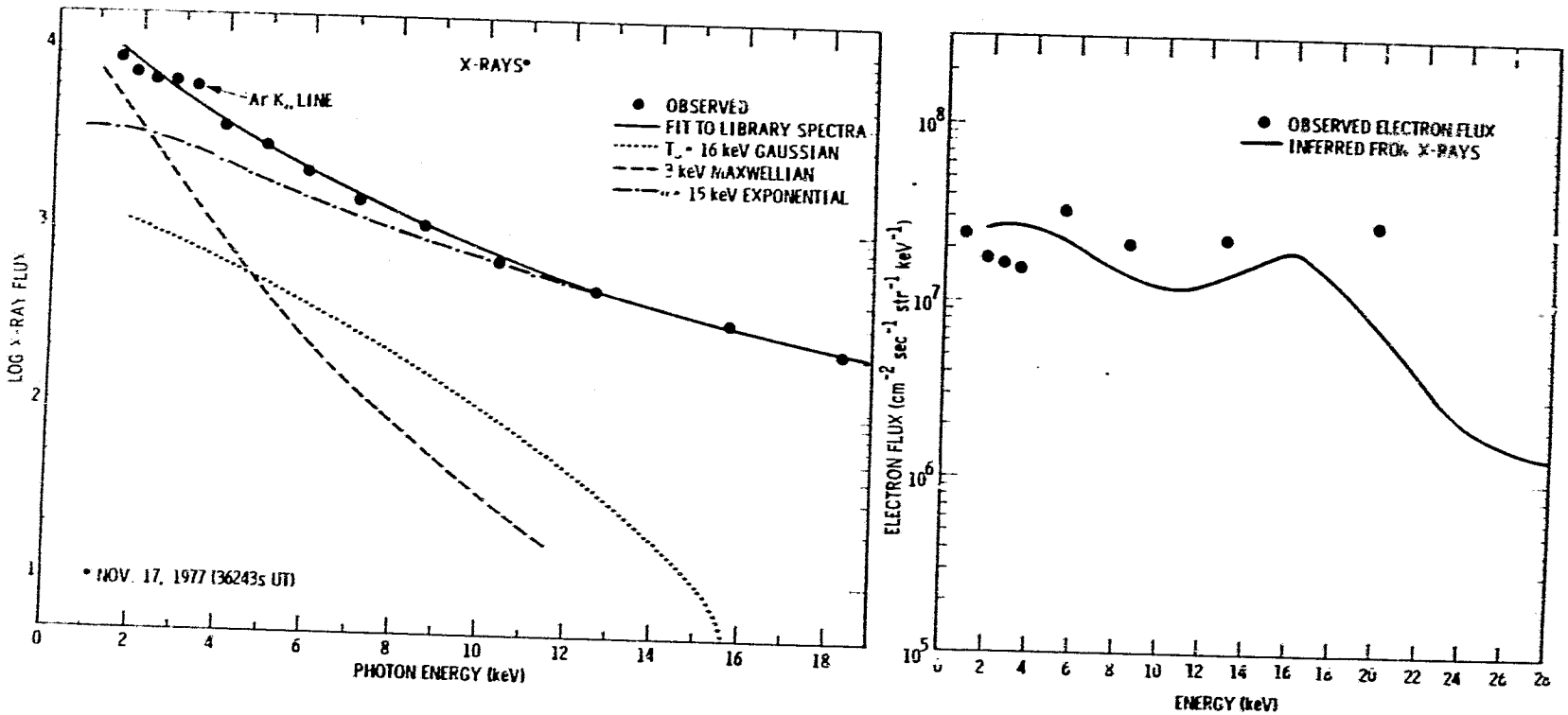
X-RAYS*
Ar K$_{\alpha}$ LINE
OBSERVED
FIT TO LIBRARY SPECTRA
T$_e$ = 16 keV GAUSSIAN
3 keV MAXWELLIAN
15 keV EXPONENTIAL
* NOV. 17, 1977 (36243s UT)
LOG X-RAY FLUX
PHOTON ENERGY (keV)
OBSERVED ELECTRON FLUX
INFERRED FROM X-RAYS
ELECTRON FLUX (cm^{-2} sec^{-1} str^{-1} keV^{-1})
ENERGY (keV)

Figure II-6: Auroral X-ray and background X-ray spectra. The structures from which the auroral spectra arise are described in the text. The background spectra are: X-rays from the sunlit Earth at times of high solar activity (S), diffuse cosmic (C) and atmospheric (A) X-rays.

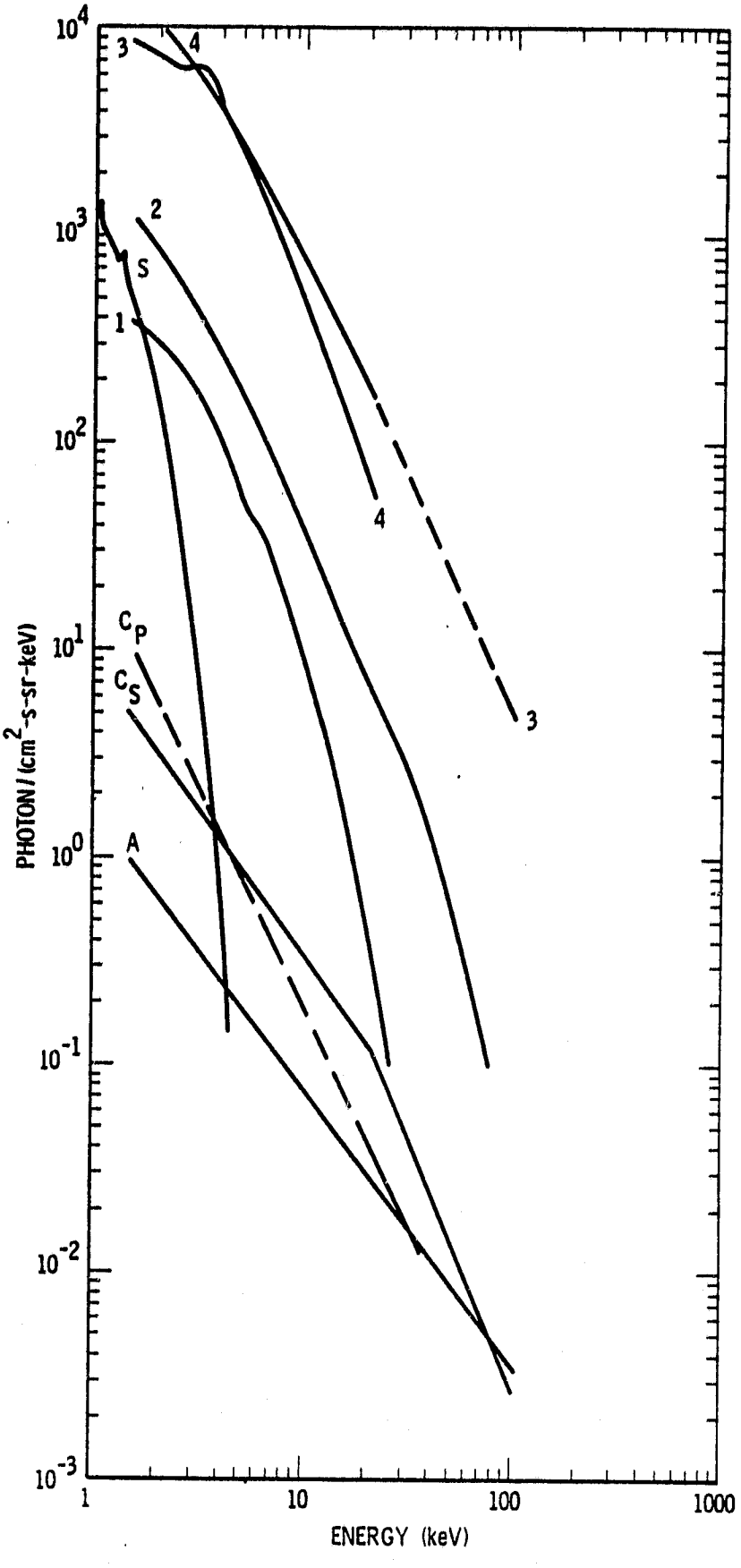
PHOTON/(cm^2-s-sr-keV)
ENERGY (keV)
10^4
10^3
10^2
10^1
10^0
10^{-1}
10^{-2}
10^{-3}
1
10
100
1000
3
4
2
S
1
4
3
C_P
C_S
A

The first term is the Gaussian, the second the 3 keV Maxwellian, and the third the high-energy tail. The parameters to be determined are T_0, σ, A, B, C, and α. A technique which can be used is to compute a library of X-ray spectra that would arise from electron spectra of the assumed form. In cases where C is not zero, C and α may be determined easily from observations at energies above about 20 keV. It is therefore important for the instrument to be sensitive to high energy X-rays. The remaining parameters are determined by comparing the measured X-ray spectrum to the library spectra. It may be necessary to restrict the number of free parameters by, for example, setting σ to 2.0 keV, a value found for two of the spectra reported by Mizera et al. (1978).

As an example of the technique described above we consider Spectrum 3 in Figure II-6 (J. G. Luhmann and M. Walt, private communication). The X-ray spectrum is plotted in the left half of Figure II-5. The peak near 3 keV is due to argon Kα emission. This should be corrected for before the fitting procedure is applied. The heavy line shows the best fit library spectrum to the data (σ restricted to 2 keV), and the other lines show the separate components of the library spectrum. On the right the observed electron spectrum is compared to the spectrum inferred from the X-rays. The agreement is very good in the energy range (< 20 keV) where both electron and X-ray data exist. X-ray measurements to higher energies are clearly desirable.

We have demonstrated a technique for deriving the electron spectrum from bremsstrahlung X-ray measurements. As more electron spectral measurements become available, the library spectra judged appropriate for fitting may be changed. The analysis undertaken here will not be applicable to all observations, since the data may be degraded by poor statistics or high background. However, in most cases it should be possible to distinguish the three compo-

nents of the electron spectrum: the plasma sheet Maxwellian, the electrons accelerated by parallel electric fields, and the high energy outer belt electrons.

In the visible range of the electromagnetic spectrum the aurora takes on a variety of forms (Davis 1978). X-ray observations with the DMSP F2 experiment display a similar variety of forms and a wide range of spectra. Mizera et al. (1978) describe a number of forms and spectra observed on a single pass of the DMSP satellite over the auroral zone on 1979 October 19. Other, unpublished, DMSP data reveal spectra both stronger and weaker than those of October 19; the observed range is more than a factor of 30 near 2 keV. In what follows we set forth representative spectra and associated spatial distributions for auroral X-ray emission. The choice of representative source spectra and morphology is of great importance because of its impact on the sensitivity and attainable spatial resolution of any experiment. The DMSP F2 X-ray experiment provides the only available data base for soft (2-20 keV) X-ray auroral spectra. All of our sample spectra are based on observations by this instrument. We believe that these spectra and the associated auroral forms shown in the visible photographs are indeed typical and can be used to evaluate candidate detector systems. In addition the background from cosmic X-rays, atmospheric X-rays and solar X-ray interactions in the atmosphere is presented. These spectra are based upon the published literature and, in the case of solar X-rays, on our own observations and calculations.

Figure II-6 shows a collection of auroral X-ray and background differential energy spectra. First we will concern ourselves with the (numbered) auroral spectra. We believe spectrum 1 to be typical of broad auroral emissions during relatively quiet times, although it is difficult to be certain of this because of the small fraction of DMSP data that has been analyzed to

date. That such emission can be widespread is illustrated in the photograph and spectrogram of Figure II-1. The three horizontal lines on the photograph show the ground track and the extent (FWHM) of the X-ray sensor field of view. The outer lines are separated by 375 km at auroral altitudes. In our simulations we assume that spectrum 1 occupies a semicircular band between 63° and 68° latitude. This constitutes Source 1.

Spectrum 2 is case 5 discussed by Mizera et al. (1978). Figure II-2 is a spectrogram and photograph used in that paper. The authors fitted a low energy Gaussian with central energy T_0 and half width σ and a Maxwellian with kT = 3 keV to five electron spectra observed on 1977 October 19. One of the authors (Luhmann, private communication) has interpreted the weaker higher energy emission with a flatter spectrum to be associated with diffuse emission during active periods. The measurements at 5538 seconds, approximated here as spectrum 2, had a relatively small Gaussian component and have been taken as typical of diffuse emission during active periods. Our curve for spectrum 2 is drawn through the data in Figure 3 of Mizera et al. (1978) and not through the curve the authors derived from their best fit electron spectrum. The assumed form in our simulations is a quarter-circle band between latitude 60° and 63°. This is Source 2.

Spectrum 3 is the spectrum of a westward traveling surge. The DMSP photograph and X-ray and electron spectrograms are shown in Figure III-3. The spectrum is interesting in that argon K X-ray line emission is apparent as a bump near 3 keV. This spectrum and the morphology shown in the visible photograph constitute Source 3. For each orbital height considered the solid angle of emission is determined by measurement on a blow-up of the optical image.

Figure II-4 shows DMSP data for a number of "inverted V" spectra as can be seen in the electron spectrograms in the two bottom panels. Two spectra, those at UT 50347-56 seconds and 50569-90 seconds, have very similar characteristics while a third, at 50509-12 seconds, is only about half as intense as the others. Spectrum 4 in Figure II-6 is the UT 50569-90 seconds spectrum and is representative of low latitude "inverted V" structures. We believe that it is associated with the well-defined arc crossing the detector center line at about UT 50580 seconds. The X-ray spectrogram shows an extended response to this arc because the arc crosses the detector field of view diagonally. The arc shown in Figure III-4 is taken to be the form for this spectrum in the detector evaluations. This is Source 4.

The four numbered spectra in Figure II-6, along with the associated spatial distributions, constitute a data base adequate to test the capabilities of instrumentation designed for auroral X-ray imaging. The background against which the imaging is to be done is also important. X-ray background spectra are denoted by letters in the figure. The spectrum labeled S results from the interaction of solar X-rays in the Earth's atmosphere for a time when the sun is active but not flaring. Curve C_p is an extrapolation of the diffuse component of cosmic X-rays from the spectrum of Pal (1973) and C_S is the same spectrum from Schwartz and Gursky (1974). Curve A is an extrapolation of the diffuse atmospheric spectrum at high latitudes reported by Imhof, Nakano, and Reagan (1976). Although all of these spectra except, in some cases, that of the sunlit Earth are weak compared to auroral X-ray spectra at energies above 1 keV, the background emission can occupy a large solid angle compared to the auroral emission. Furthermore, except for the solar X-rays, all the background spectra are flatter than the auroral spectra and therefore become more important with increasing energy.

The major task in studying the background spectra is the computation of the spectrum resulting from the interaction of solar X-rays in the sunlit Earth's atmosphere. Solar X-rays can scatter in the Earth's atmosphere or produce characteristic nitrogen and oxygen (and during flares, argon) K X-rays by fluorescence (Rugge, McKenzie, and Charles, 1979). We have used data from the Aerospace X-ray Spectrometer/Spectroheliograph on the U.S.A.F. Space Test Program P78-1 satellite to estimate the X-ray emission from the entire Earth-facing solar hemisphere during a period of high solar activity but in the absence of flares. Then, by using the techniques that successfully modeled the X-ray spectrum of the sunlit Earth observed by the HEAO A-1 experiment (Rugge, McKenzie, and Charles 1979), we computed the X-ray spectrum arising from the interaction of solar X-rays in the atmosphere. The CIRA 65 model 7 at local noon was used to model the atmospheric densities. The spectrum observed depends upon the Sun-Earth-detector geometry as well as the incident spectrum. We used a variety of geometries corresponding to local noon observations by a high altitude satellite. Curve S is the most intense spectrum obtained, but other summer spectra were almost as strong. The curve should be taken as an upper limit because we may have overestimated the typical solar active region temperature by as much as 10^6 K. In the event of such an overestimate the curve exaggerates the sunlit Earth's spectrum by a factor of 2.5 at 2 keV and 10 at 3 keV. Despite these uncertainties, it can be seen that secondary X-rays from the sunlit atmosphere can be an important source of background below 2-3 keV when the sun is active. At quiet times the spectrum may be a factor of 50 below Curve S at 1 keV. Such weak spectra were observed by HEAO-1.

The other background spectra are better known, and we have taken them from the literature. The atmospheric background spectrum, A, is an extrapola-

tion below 40 keV of the high latitude emission measured by Imhof, Reagan, and Nakano (1976). In deriving their spectrum, these authors corrected for the diffuse component of cosmic X-rays by using the spectrum of Pal (1973). The curve C_P is an extrapolation of Pal's spectrum. In our studies we will use the diffuse cosmic X-ray spectrum, C_S, compiled by Schwartz and Gursky (1974), since it involves no extrapolation in our energy range of interest.

Since most of the instruments to be discussed in the following sections use large-area proportional counters as detectors, we need to estimate the internal background of such a detector. We base the estimate on the HEAO-1 detector performance reported by Rothschild et al. (1979). The HEAO-1 detector background suppression was accomplished by anticoincidence techniques in a multiwire counter. The HEAO-1 MED (medium energy detector) had a background rate of 7×10^{-3} cm^{-2} s^{-1} in a 1.5-20 keV band, and HED 3 (high energy detector 3) had a background rate of 6×10^{-3} cm^{-2} s^{-1} in a 2.5-6 keV band and 3×10^{-3} cm^{-2} s^{-1} in an 8-70 keV band. Less than one-half of the background events are attributable to internal detector background. We wil be considering two energy bands: 2-5 keV and 10-20 keV. Based on the above figures we assign a background of 3×10^{-3} cm^{-2} s^{-1} to the former band and 4×10^{-3} cm^{-2} s^{-1} to the latter. Both figures are somewhat higher than the HEAO-1 figures.

III. CANDIDATE INSTRUMENTATION

In this section we specify and analyze auroral X-ray imaging instrumentation. The candidate systems are: X-ray telescope, pinhole camera, coded aperture, rastered collimator, and imaging collimator. We place limits on the size and weight of the systems to be certain that the experiments are practical for high altitude satellites. The limits are: maximum length along the optical axis, 75 cm, and maximum mass, 30 kg. These limits are compatible with a modest-sized satellite that must be raised to high orbit. Considerations regarding detection and imaging techniques and the physical configuration of individual detection systems are specified in sufficient detail to permit realistic performance evaluations and intercomparisons. Obviously other configurations are possible, but the extension of the results of the analysis to such cases should be relatively easy. We place no limits on telemetry, but will call attention to any unusually high requirements. High bit rates might, of course, be reduced by special data packing or on-board processing. We do not expect power to be a problem.

A. X-Ray Telescope

The index of refraction of all materials is less than one at X-ray wavelengths. This implies that, if the glancing angle of incidence is less than some critical value characteristic of the material and the X-ray energy, X-rays will be totally reflected. The critical angles for X-rays in the keV range are small, on the order of 1-2 degrees. However the reasonably high reflectivity that can be obtained at small glancing angles of incidence is the basis for the development of imaging X-ray optics.

The simplest focusing device is a paraboloid of revolution. This focuses on-axis X-rays at the focus of the parabola, but X-rays incident off-axis are brought to an annulus around the focus; no imaging is possible. The Abbe sine condition is grossly violated. Wolter (1952) showed that by using two reflections one can satisfy the Abbe sine condition and obtain an image. He also displayed a number of configurations for X-ray microscopy, based upon paraboloids, hyperboloids, and ellipsoids of revolution. From these the glancing incidence X-ray-EUV telescope has been developed.

The Wolter type I telescope is the one that is useful in the keV and sub-keV X-ray region. The telescope consists of a paraboloid and a hyperboloid with a common focus. On-axis X-rays strike the paraboloid and are reflected toward the common focus. Before reaching the focus they strike the hyperboloid and are reflected toward its second (and nearer) focus. The arrangement is shown in Figure III-1.

The X-ray telescope has three main virtues for auroral imaging. First, a high quality image is formed. Astronomical X-ray telescopes commonly have angular resolution of a few arc seconds. It is doubtful that one could do as well for auroral observations since a wide field of view is required and much of the scene will be far off axis. Although the resolution of an X-ray telescope degrades off-axis (e.g., Viana 1978), it would still be much better than that provided by any other system considered in this study. The X-ray telescope's second advantage is that the effective area can be substantially larger than the detector area. The third is that the detector is buried in the satellite and there is no direct path to it from the outside. These last two factors make background reduction easy.

Figure III-1: X-ray telescope geometry. X-rays enter from the right and are imaged around the focus after striking the paraboloid then the hyperboloid. After Mangus and Underwood (1969).

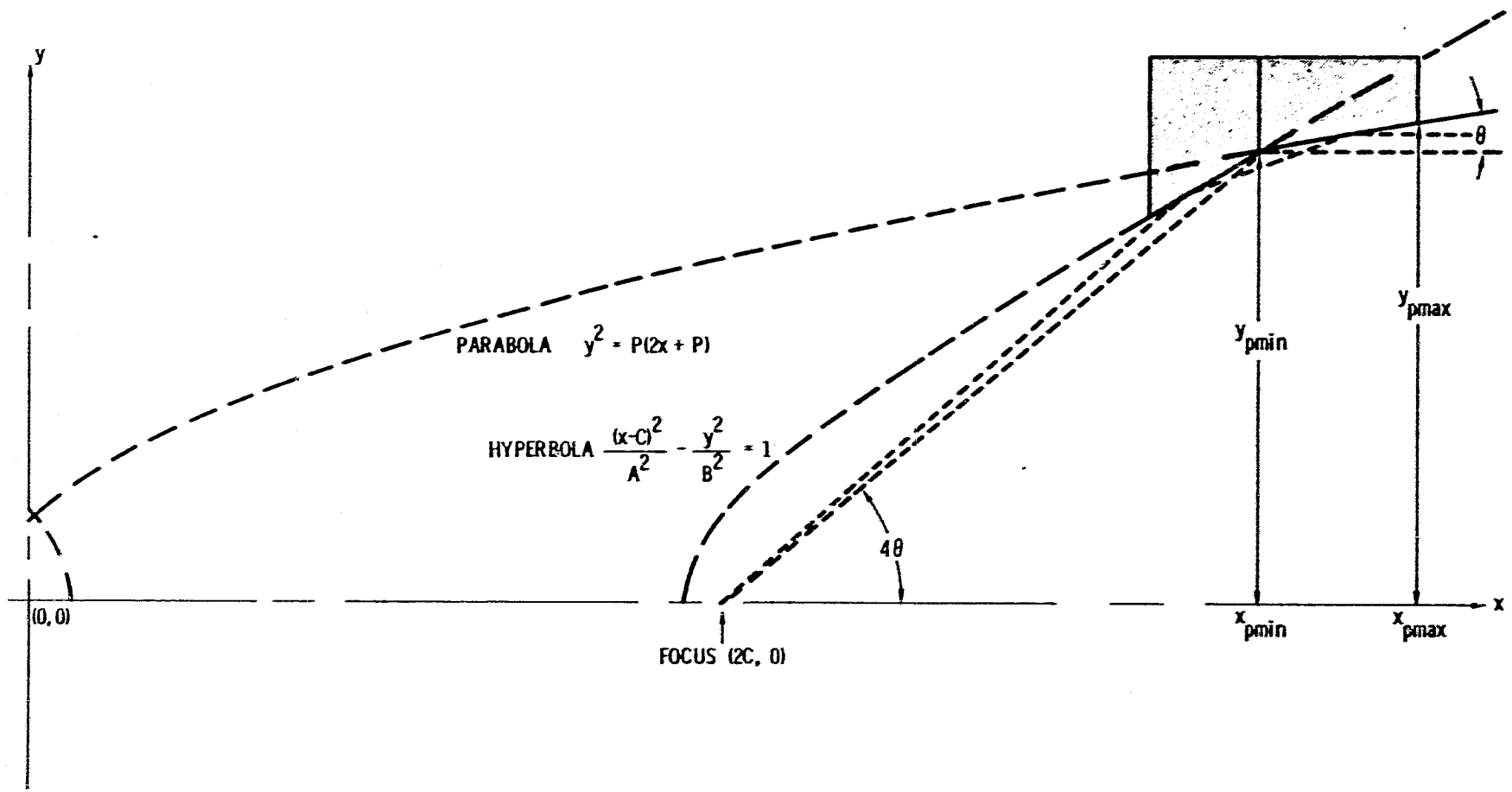
y
PARABOLA $y^2 = P(2x + P)$
HYPERBOLA $\frac{(x-C)^2}{A^2} - \frac{y^2}{B^2} = 1$
θ
4θ
y_{pmin}
y_{pmax}
(0, 0)
FOCUS (2C, 0)
x_{pmin}
x_{pmax}
x

In order for an image to be obtained in a reasonable amount of time it is desirable for the X-ray telescope to have a large field of view. Even from a distance of 15 R_E the circle at 60° latitude has a radius of about 2°. Thus, to image with a single pointing, the telescope must have a field of view diameter of at least 4°. This also means that the on-axis angle of incidence should be at least 2° or the off axis radiation would miss much of the telescope surface. The use of such a high angle of incidence limits the useful energy range severely.

An auroral X-ray imaging system should operate over as wide an energy range as possible so that the X-ray spectrum, and hence the electron spectrum, can be deduced. An X-ray telescope can operate at sub-keV energies. It has the potential for measuring X-ray spectra in an as yet unexplored low energy region if a satisfactory detector can be developed. On the other hand the X-ray telescope has a severe disadvantage in its inability to measure spectra above about 4 keV. This limitation prevents the unfolding of the important keV range electron spectrum. In our opinion it makes the X-ray telescope unsuitable as an auroral X-ray imager. Nevertheless, we shall specify a sample system and analyze its imaging properties. A telescope might be used in conjunection with one of the other systems to be discussed below, but this would require a larger total instrument package than those under consideration here.

In order to evaluate the performance of an X-ray telescope for auroral X-ray imaging we have to have an estimate of the parameters of a sample system. It is not our purpose to design a system but only to estimate the effective area, as a function of energy, that might be available. We will follow the formulation of Mangus and Underwood (1969). We specify that the overall experiment is to be 75 cm long and allow 3 cm behind the focal plane for

detector structure, leaving an overall telescope length of 72 cm. We refer to Figure III-1. The angle of incidence, θ, is defined for on-axis radiation reflected from the two surfaces at their intersection. We specify that the angle of incidence for this ray is θ for both the paraboloid and the hyperboloid. Since the ray is deflected by 2θ at each reflection, the angle at the focus is 4θ, as shown. The focal length, f, is the distance between the focal point and the hyperboloid-paraboloid intersection. The projected area of the telescope is $\pi\ (y^2_{pmax} - y^2_{pmin})$. Using the equation of the paraboloid,

$$y^2 = p(2x + p) \quad , \tag{2}$$

we have

$$A = 2\pi p(x_{pmax} - x_{pmin}) = 2\pi p \ell_p \quad , \tag{3}$$

where ℓ_p is the length of the paraboloid. Differentiating equation (2) we have

$$\tan\theta = \frac{p}{y_{pmin}} = \frac{p}{f\sin 4\theta} \quad . \tag{4}$$

Substituting from equation (4) for p into equation (3) we have

$$A = 2\pi f \ell_p \sin 4\theta \tan\theta \approx 8\pi f \ell_p \theta^2 \quad . \tag{5}$$

This is a very good approximation since θ is a small angle. Because two reflections occur, both at about the same angle, the effective area is

$$A = 8\pi f \ell_p \theta^2 \epsilon^2(\theta, h\nu) \quad , \tag{6}$$

where $\epsilon(\theta, h\nu)$ is the reflection efficiency, a function of both θ and the X-ray energy, $h\nu$. We specify that θ is to be 2°. The length limit amounts essentially to the condition, $f + \ell_p = 72$ cm. The area would be maximized for $f = \ell_p$, but the length of the paraboloid cannot be increased without also increasing off-axis aberrations (Van Speybroeck 1979). We therefore choose, somewhat arbitrarily, a focal length of 60 cm. This specifies the mirror geometry completely. The geometrical projected area is 23.1 cm^2. The total area can be increased by nesting other mirrors inside at 2 cm intervals. These inner mirrors have smaller incidence angles, so they reflect efficiently at higher energies but have small fields of view. The angles of incidence are 1.52°, 1.04°, and 0.56°, and the total projected area of all four mirrors is 43.7 cm^2.

The effective area of the telescope depends on the surface coating of the mirrors. Astronomical X-ray telescopes commonly have a nickel surface. An alternative with reasonably high reflectivity at large angles of incidence is gold. We calculated the effective area of our sample system for both nickel and gold surfaces using reflectivity data published by Gursky and Schwartz (1974). While the gold provided a slightly larger area at 1 keV, the nickel was substantially better around 2 keV and about equal to gold at higher energies. We chose nickel as the surface material. Figure III-2 is a plot of the overall effective area as a function of energy with off-axis angle as a parameter. For the off axis angles, we simply summed the effective area of all of the individual two-mirror telescopes having an angle of incidence for on-axis radiation that is smaller than the off-axis angle. We re-emphasize that the sample system shown here has not been optimized with regard to image quali-

Figure III-2: Computed effective area as a function of X-ray energy and off-axis angle for the sample X-ray telescope described in the text.

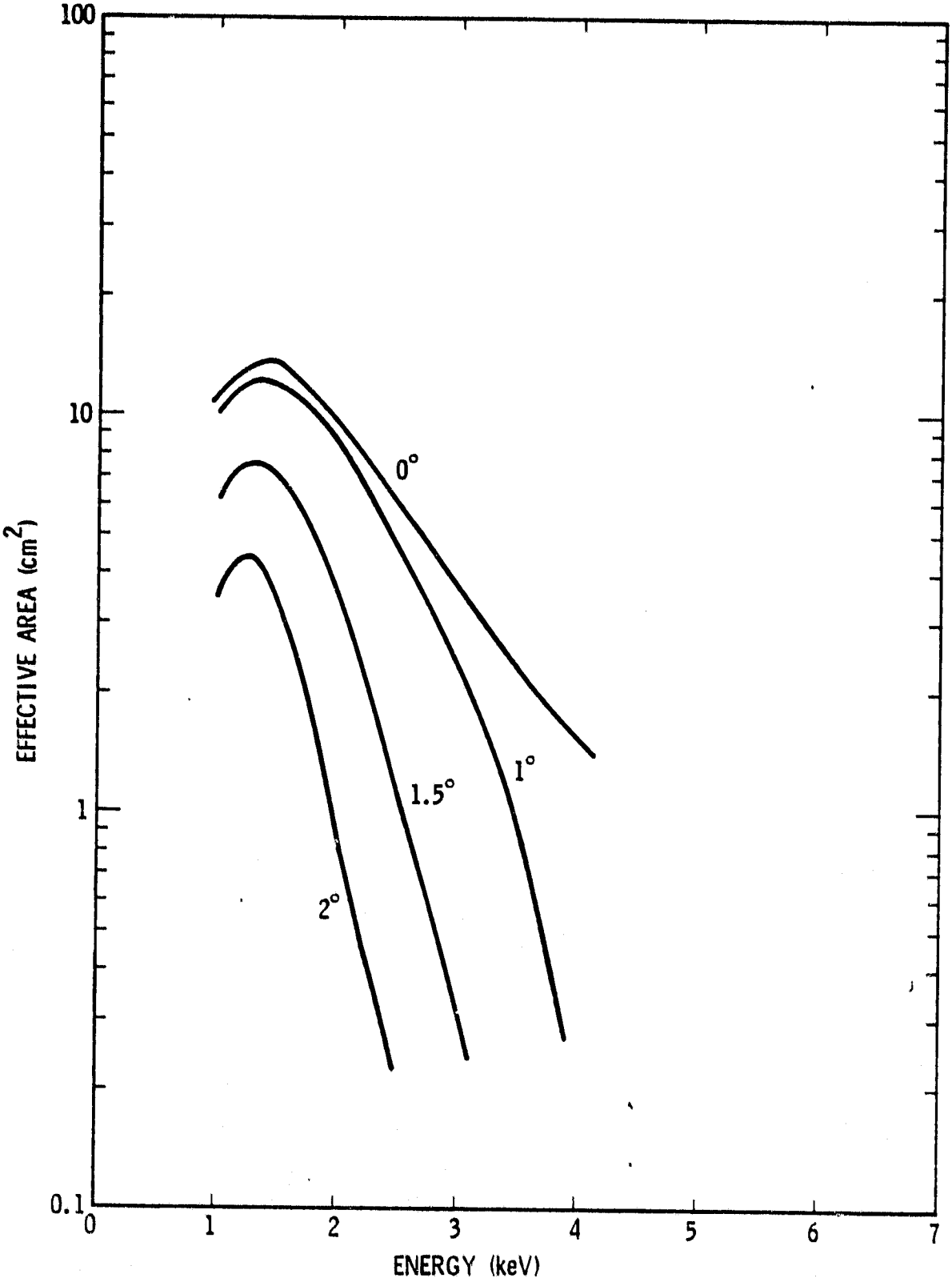
100
10
1
0.1
0
1
2
3
4
5
6
7
EFFECTIVE AREA (cm^2)
ENERGY (keV)
0°
1°
1.5°
2°

ty. We believe, however, that the effective areas in Figure III-2 are typical of what can be achieved.

The sample system has been specified to comply with the maximum overall length limit of 75 cm. A simple calculation indicates that the mass restriction of 30 kg will be met. The outside radius of the telescope can be made less than 11 cm, and the mirror length is about 24 cm. A solid cylinder of aluminum or quartz of the above size has a mass of about 24 kg. Thus the mirror mass should be less than 24 kg, and the total experiment weight should be less than 30 kg.

We now consider the sensitivity of an X-ray telescope as an auroral imager. The effective area falls off rapidly with increasing energy. In fact, this fall-off is so rapid that it appears to be advantageous to abandon the attempt to measure the X-ray spectrum. If we are concerned only with event counting we can use a charge coupled device (CCD) in an integrating mode as a detector. This allows much better spatial resolution than would a position sensitive proportional counter. Ideally, one would like to use a CCD as a single photon counter and retain the spectral information, but as yet the CCD technology is not sufficiently developed for that use (Catura and Smithson 1979, Schwartz et al. 1979). To limit the dark current, the detector should be cooled to around -60° C and read out about once per second (Schwartz et al. 1979). Note that with a 60 cm focal length a field of view of 2° radius would require a CCD or mosaic of CCDs having a dimension of about 4 cm.

We consider observations from three radial distances (measured from the center of the Earth): $4R_E$, $9R_E$, and $15R_E$. We have integrated the sample auroral spectra times the telescope effective area from 1-5 keV. The detector is considered to have unit efficiency and background is assumed to be negli-

gible. We require a 3σ detection (i.e., 9 photons) in a 300 s observation. For $15R_E$ the telescope has sufficient field of view (FOV) that a single pointing of 300 s will suffice. Closer to the Earth the instrument requires multiple pointings: at $9R_E$ four pointings of 75 s each are required, and at $4R_E$ sixteen of 18.75 s each are required. The results are given in Table III-1. For each case a certain emitting solid angle is required to provide 9 counts in a single pointing. In the table this solid angle is assumed to be in the form of a square, and the side of that square, in km at the Earth, is the tabulated quantity. This can be regarded as the limiting spatial resolution for a given observation. The spatial resolution obtained for source #4 at 4 R_E corresponds to a pixel of 2.07×10^{-6} sr. If the auroral zone is taken to be inside of a circle at 60° latitude, its solid angle from $4R_E$ is 7.85×10^{-2} sr. Thus about 3.8×10^4 pixels of the minimum size found would be required. If each is read out with 8 bits every 100 seconds the telemetry requirement would be 3 kbit-s^{-1}. Actually, the ability to have somewhat better spatial resolution for very intense events is desirable. This might raise the desired telemetry allowance to as much as 10 kbit-s^{-1}. This should not be regarded as excessive. Table III-1 shows that the X-ray telescope can be expected to have adequate sensitivity and spatial resolution to image well most auroral sources. Its imaging ability is, in almost all cases, superior to that of the other instruments to be discussed below.

In summary, the X-ray telescope offers the ability to obtain a high-quality image of the aurora at energies below about 3-4 keV. In addition it can obtain spectral information in the unexplored sub-keV region, but to do so requires a different detector arrangement than has been discussed above. The use of a CCD as a single photon X-ray detector may be developed to a sufficient degree in the next few years to fulfill this requirement. The very poor

Table III-1

X-Ray Telescope: Achievable Spatial Resolution (Square Pixel)

Spectrum #	Orbit (R_E)	Off-Axis Angle (degrees)	Spatial Resolution (km)
1	15	0	192
		2	415
2	15	0	109
		2	228
3	15	0	38
		2	86
4	15	0	32
		2	70*
1	9	0	222
		2	480*
2	9	0	126
		2	264
3	9	0	44
		2	99
4	9	0	37
		2	80*
1	4	0	171
		2	370**
2	4	0	97
		2	203
3	4	0	34
		2	76
4	4	0	29
		2	61*

*Pixel size larger than smallest spatial dimension of source

**No spatial resolution advantage over pinhole camera or coded aperture

sensitivity above 4 keV (essentially zero above 6 keV) means that the X-ray telescope cannot obtain sufficient spectral information to unfold the auroral electron spectrum. This is the first step in obtaining physically meaningful results from an X-ray imaging experiment. Thus the X-ray telescope alone is an incomplete experiment.

B. Pinhole Camera

Figure III-3 illustrates the multiple pinhole camera concept. The camera consists of a plate with an array of pinholes and a position-sensitive detector. The pinholes are arranged so that the images of the observed regions do not overlap. If the pinholes are arranged to provide nonoverlapping images of the auroral oval, each image will receive photons from diffuse cosmic or atmospheric X-ray emission through holes other than its own. Thus it is usually desirable to add vertical baffles to the pictured camera in order to limit the number of holes contributing background in each image. These baffles are omitted from the figure for the sake of clarity.

The effective area of the pinhole camera is equal to the area of each pinhole times the number of pinholes open. The spatial resolution is no better than the hole diameter, d, divided by the "focal length", f, the distance between the pinhole and the image plane at the detector. In practice the position sensing resolution of the detector further degrades the instrument spatial resolution beyond the lower limit of d/f. If the object being viewed is large compared to the camera's spatial resolution, considerable gain can be realized by enlarging the hole. Doubling the hole diameter quadruples the effective area, quadruples the solid angle in the (now larger) resolution element and doubles the minimum achievable spatial resolution. The result is that the signal in a single picture element (pixel) can increase sixteen-fold

Figure III-3: A multiple pinhole camera.

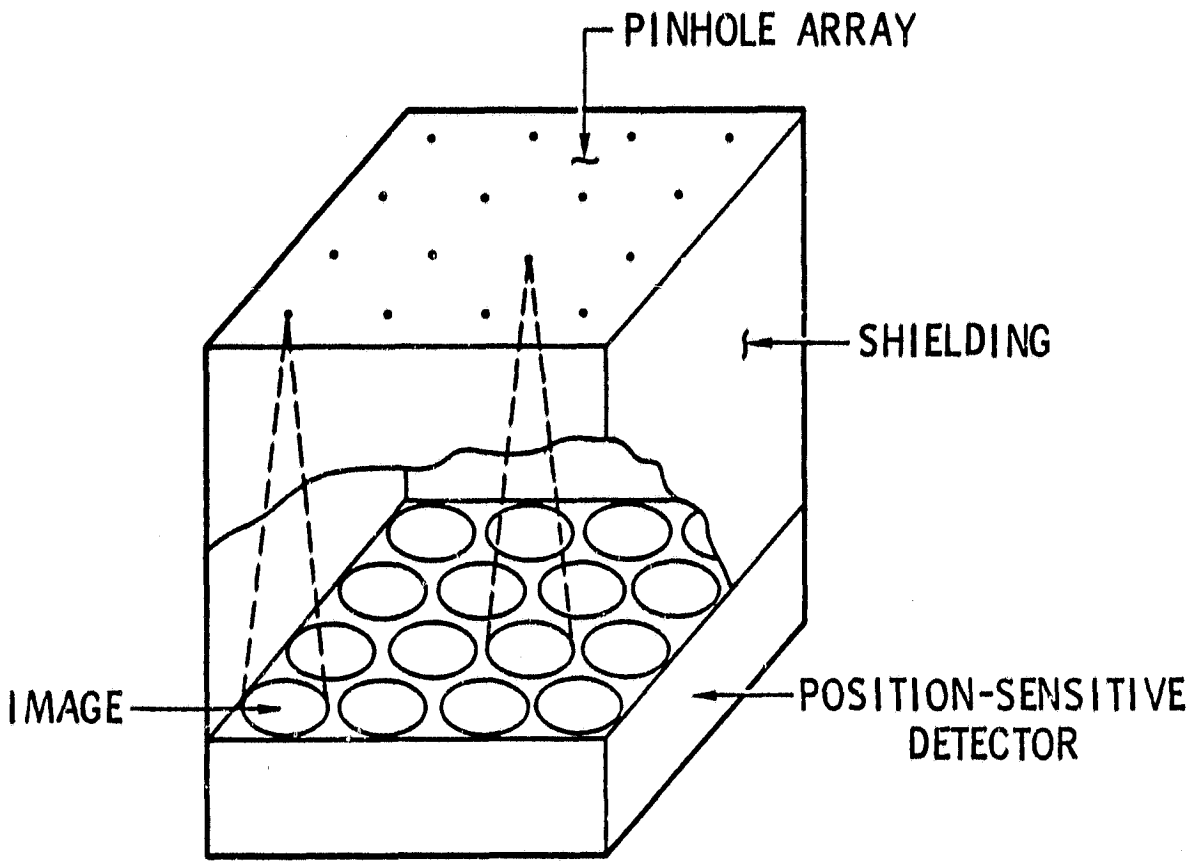
PINHOLE ARRAY
SHIELDING
IMAGE
POSITION-SENSITIVE
DETECTOR

while the noise quadruples for a four-fold increase in the single pixel signal to noise ratio (SNR). If the pinhole size cannot be adjusted the best one can do along similar lines is to add the counts from four adjacent pixels for a doubling of the SNR. Thus it is desirable to have an adjustable pinhole diameter. Similarly if the instrument is to be used at various heights (elliptical orbit or different orbits in the same mission) it is desirable to be able to vary the number of pinholes and their spacing. This is because the image diameter decreases as the satellite height increases. The only consideration is assuring that the images never overlap. Techniques for accomplishing a variable aperture configuration can be readily imagined.

The detector for the multiple pinhole camera, and for the coded aperture to be discussed in the next section, would be a large area position-sensitive sealed proportional counter. As discussed in Section II, measurement of the spectrum to at least 20 keV is important for extracting the auroral electron spectrum, and operation at even higher energies is desirable. For this reason, the detector is made with a depth of 6 cm and a gas fill of 1.5 standard atmospheres of xenon with a CO_2 quench. Xenon provides a high detection efficiency for energetic X-rays. A thin beryllium window can be used. For example, one of the detectors in the Aerospace Bragg crystal spectrometer experiment on the U.S.A.F. Space Test Program P78-1 satellite has an unobstructed area of 27.4 cm^2, a gas fill of 1.1 atmospheres of argon-CO_2, and a 1.1 mil (2.8×10^{-3} cm) Be window. Here we are considering a much larger area and somewhat higher internal pressure so a thicker window is required. We will use a 1.0×10^{-2} cm (4 mil) beryllium window. The window will be supported with beryllium rods which will become transparent to X-rays above about 10 keV. The detector efficiency as a function of energy is plotted in Figure III-4.

Figure III-4: Efficiency of the large area proportional counter used in the various instrument studies in this section.

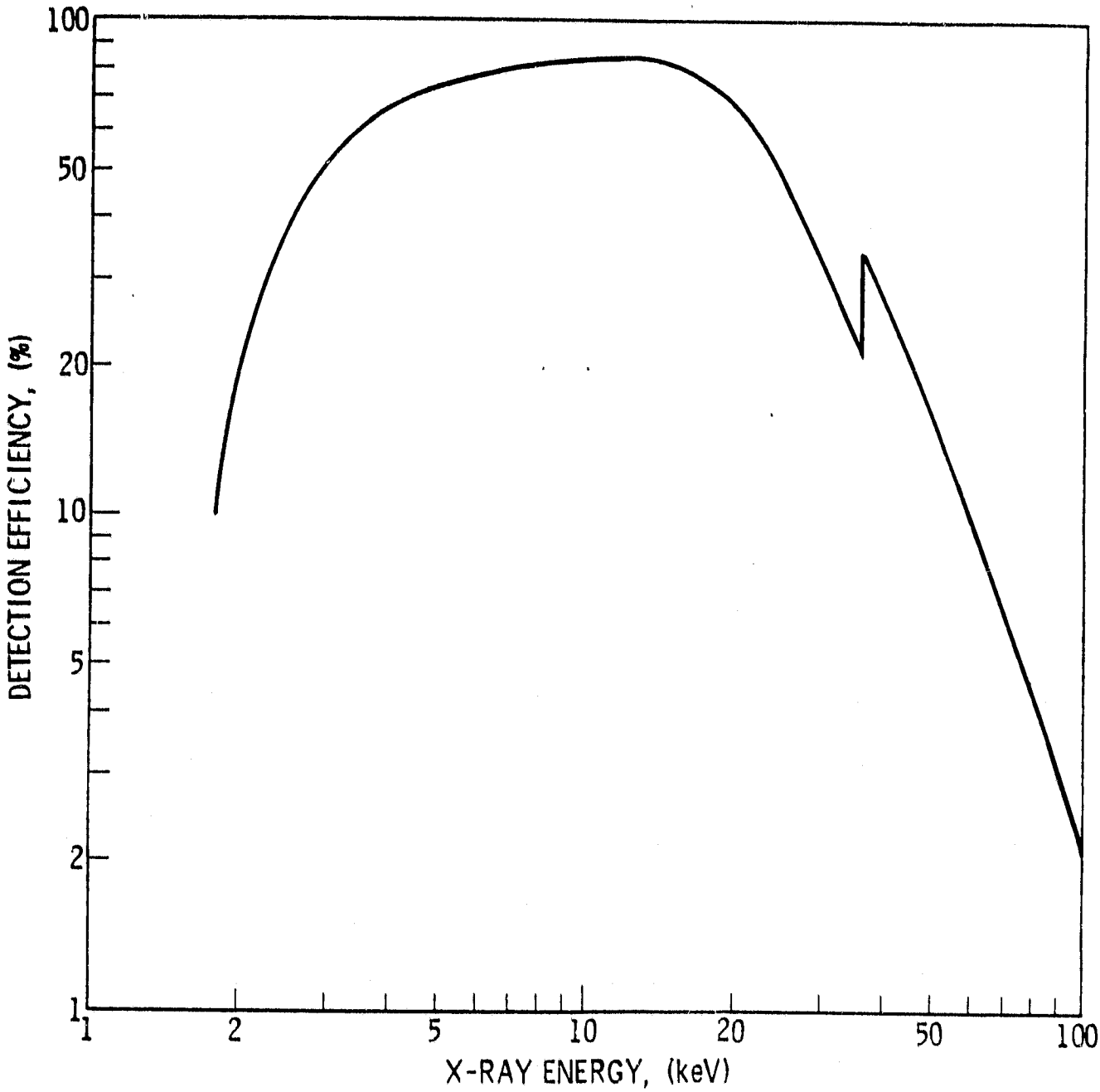
100
50
20
10
5
2
1
DETECTION EFFICIENCY, (%)
1
2
5
10
20
50
100
X-RAY ENERGY, (keV)

The event detection is accomplished by planes of closely spaced anode wires. Position detection along the anodes can be accomplished by analyzing signals induced in cathode wires arranged in a plane and running perpendicular to the anodes. We estimate that a position resolution of 2 mm would be easy to achieve in each dimension over a large area by this technique. Long et al. (1979) achieved a resolution of a fraction of a millimeter near the center of a large area counter, with degraded resolution near the edges. Because of the large counter depth required for reasonable efficiency it will be necessary to use more than one plane of wires. For observations as near in as $4R_E$ the X-rays can be about 9° off axis. This can result in a position uncertainty of about Stan9°, where S is the wire plane spacing. Thus to maintain 2 mm resolution S must be ~ 1.3 cm, and five detection planes are required. The use of many detection planes has the additional advantage that many anticoincidence arrangements are now possible to help achieve the internal background levels discussed in Section II. For example, high energy events in the first layer and low energy events in the back layers could be rejected with little loss in system efficiency.

The third component of the camera is the shielding. We design the system to have a thickness of 3 absorption lengths for 60 keV X-rays. This provides excellent absorption at energies only a little lower. The absorption is accomplished through the use of a "graded Z" passive shield; that is a shield whose outermost layer is of high atomic number (Z) and whose inner layers are of lower Z. Each successive layer is specifically designed to absorb the secondary characteristic X-rays of the next outer layer. We use, from the outside, tin, copper, aluminum (which provides the mechanical rigidity in addition to X-ray absorption), and a thin plastic inner coating. The total mass is 0.97 g/cm^2. This shielding material surrounds the camera on four

sides, as shown in Figure III-3, and composes the pinhole aperture plates. In addition, two internal baffles divide the pinholes into four sets in quadrants.

The sample systems can now be specified. As with the X-ray telescope we consider orbits at $4R_E$, $9R_E$, and $15R_E$. The spatial resolution used at different altitudes is determined by a number of considerations. As noted above, the detector spatial resolution should be around 2 mm. This means the minimum achievable angular resolution (with no effective area) would be about 0.2°. Above this level the sensitivity (i.e., effective area - solid angle product) increases rapidly while the angular resolution increases slowly. The similarities between the pinhole camera and coded aperture impose another constraint. In order to compare the two systems we would like to limit the variables between them by making them both have the same angular resolution. Resolution of around 0.5° gives each system reasonable sensitivity except for the detection of weak sources at high energy. As will be discussed later on, only for certain matrix dimensions (in terms of numbers of cells) can coded apertures be made. Thus, if the length f is specified, only certain angular resolutions can be obtained. Therefore the exact angular resolution of each system is determined by what can be obtained with a coded aperture.

The size of a system is determined by the available weight. After allowance for digital electronics, the pinhole adjustment mechanism and its electronics, and miscellaneous small parts, we estimate that 23 kg are available for the detector, the apertures, and the shields. We estimate that the detector and its front end electronics would have a mass of 10 g for each cm^2 of active area. As discussed above, the shielding has a mass of 0.97 g/cm^2, and there are six vertical pieces (four sides to the main shield and two baffles) and the two horizontal aperture plates. We assume that the detector is

square. A major constraint is that the images from adjacent pinholes must not overlap. If the pinhole width is d, the spacing is s, and the angular extent of the field of view is θ , the equation, $s \geq d + f\tan\theta$, must be satisfied. A focal length, f, of 50 cm was chosen for the pinhole camera, because it allows four pinholes of width up to 1.6 cm, without overlap, for the $4R_E$ set. Subject to the above constraints, the pinhole camera configurations in Table III-2 were specified.

Table III-2

Pinhole Camera Configurations

Orbit (R_E)	Resolution		# Pinholes	Pinhole Area cm^2
	Angle (deg)	Distance (km)		
4	0.57	200	4	0.99
9	0.39	350	25	2.90
15	0.51	800	64	12.68

The signal to noise ratio (SNR) for a flux measurement from a single source element by a pinhole camera is

$$SNR = \frac{\varepsilon M_0 A_p t}{[\varepsilon M_0 A_p t + \varepsilon I_d \Omega_d A_p t + B A_p t]^{1/2}} , \qquad (7)$$

where

ε = the detector efficiency,

M_0 = the flux from the resolution element being detected which is incident on the camera,

A_p = the total pinhole area (Table III-2),

t = the exposure time,

I_d = the intensity of diffuse background X-rays,

Ω_d = the solid angle for diffuse X-rays passing through remote pinholes, and

B = the internal detector background.

Equation (7) can be rewritten as

$$SNR = \frac{\varepsilon M_0 (A_p t)^{1/2}}{[\varepsilon M_0 + \varepsilon I_d \Omega_d + B]^{1/2}} \tag{8}$$

We will be concerned with the time required to make a SNR = 3 detection of a single emitting source pixel. This is given by setting SNR = 3 in equation (8) and solving for t:

$$t_3 = \frac{[\varepsilon M_0 + \varepsilon I_d \Omega_d + B]}{A_p (\varepsilon M_0)^2} \tag{9}$$

We consider detection times for the four sample spectra in Figure II-6 in two energy bands, 2-5 keV and 10-20 keV. Each spectrum, including background spectra, was multiplied by the efficiency function in Figure III-4 to obtain the quantities εM_0 and εI_d. The two baffles divide the pinhole arrays into four groups so that Ω_d is the solid angle of N/4 - 1 pinholes, where N is the total number of open pinholes during the measurement. The background, B, is discussed in Section II. It is .003 cm^{-2} s^{-1} in the 2-5 keV band and .004 cm^{-2} s^{-1} in the 10-20 keV band. The detection times are tabulated in Table III-3.

Table III-3 requires some discussion. Most of the sources are detectable in the 300 seconds that is a desirable duration for an auroral observation.

Table III-3

Pinhole Camera SNR = 3 Detection Times

Orbit (R_E)	Source	Resolution (km)	t_3 (2-5 keV) (sec)	t_3 (10-20 keV) (sec)
4	1	200	445	1.1×10^4
4	2	200	163	803
4	3	200	11	30
4	4	200	43	279
9	1	350	383	1.5×10^4
9	2	350	158	985
9	3	350	11	29
9	4	350	61	495
15	1	800	92	4.2×10^3
15	2	800	56	410
15	3	800	4	11
15	4	800	25	256

The observations are almost all photon, rather than background, limited. In many cases the auroral forms are not resolved by the camera. The narrow dimensions of the objects are: Source 1, 480 km; Source 2, 290 km; Source 3, ~ 230 km (irregular); and Source 4, ~ 50 km. The unresolved objects cannot be resolved through use of smaller pinholes. In the cases of Sources 1 and 2 the sensitivity would be poor if the pinhole area were substantially reduced, and for the other sources the minor dimensions are near or below the basic limits set by a detector spatial resolution of 2 mm. On the other hand the detectability of Source 1 can be improved by sacrificing spatial resolution. For example, at 4 R_E the pixel size can be doubled and still be comparable to the size of the object. The detection times (first line of Table III-3) become 25 s and 359 s. Similarly, for Source 2, if the pixel dimension increases by a factor of 1.5 the pixel will be ~ 90% filled, and the detection times will be reduced to 35 and 157 seconds. The long exposure times for Source 1 for high altitude observations cannot be reduced to the few hundred second range. There simply is very little emission above 10 keV in this case.

In summary, the pinhole camera can provide spectral observations and images of most auroral forms out to energies of 20 keV or more with exposure times of a few hundred seconds or less. Narrow arcs and similar objects are not spatially resolved, even from relatively low altitude. However an image allows one to get a good overall picture of auroral activity throughout the polar region. Successive images with different spatial resolution, made possible by the pinhole size variability, allow the experimenter to obtain the best available resolution on bright objects and then to detect faint objects that would not be visible at high resolution. What is most important, the X-ray spectrum can be determined as a function of position in the auroral oval. This then allows the extraction of electron spectra, the first step in the analysis of auroral phenomena on a global scale.

The pinhole camera with a variable aperture is easily adaptable to operation in an eccentric orbit or in more than one orbit in a single mission. The decreasing field of view at higher altitudes allows more holes to be opened. In practice, accommodating two or three different pinhole patterns (for different altitudes) may result in there being fewer open pinholes than in the examples of individual systems already discussed. Thus the high altitude system may have 49 or 36 pinholes instead of the 64 in the $15R_E$ sample. Since the detection time is inversely proportional to area, some performance degradation is the cost of operational flexibility.

C. Coded Aperture

A coded aperture is a plate divided into N cells, K of which are open to transmit X-rays and the rest of which are opaque. X-rays from each source point create a shadow image of the plate on a position sensitive detector. Thus if the source is extended the shadow images overlap and the structure of the source must be recovered mathematically from the matrix of detector counts. For a single point source in the field of view the image is an exact replica of the plate. In this case the coded aperture acts as K pinhole cameras. However the signal from each point in the source creates noise at every point in the image. Thus as the source becomes more complex and extended the K-fold advantage over a single pinhole camera, which is attained for a point source, is diminished; in fact, the advantage may disappear.

Figure III-5 illustrates a coded aperture system. An N cell fundamental array the same size as the active area of the detector is at the center of the plate at the top. The field of view of the system is the angle subtended, at the detector, by this fundamental array. So that each point in the field of view can cast a complete shadow on the detector the N cell array is repeated

Figure III-5: Coded aperture geometry. The basic array is in the center box and is half repeated all around the outside. The central array has the same area as the detector.

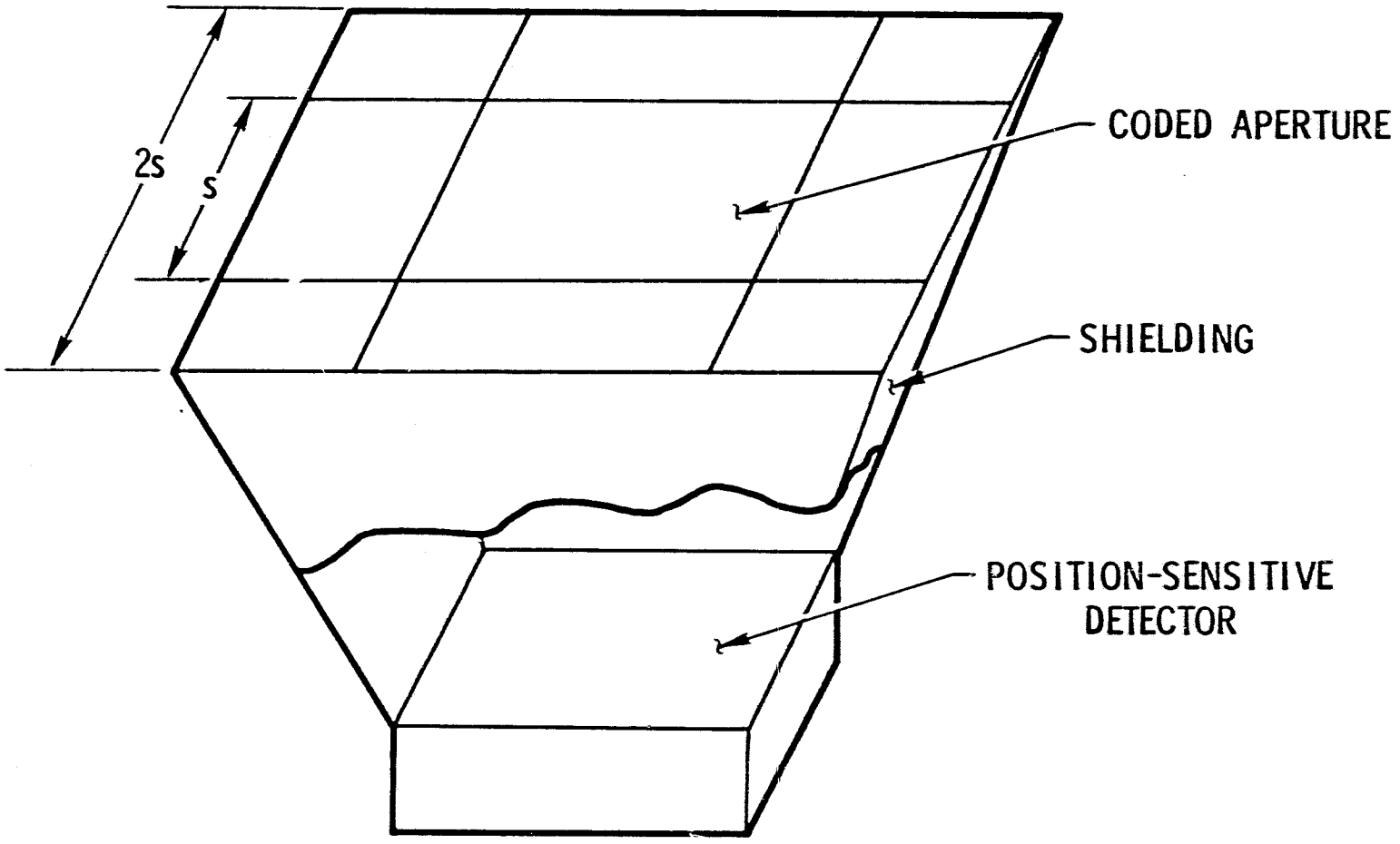
2s
s
CODED APERTURE
SHIELDING
POSITION-SENSITIVE
DETECTOR

outside the central area. Thus the central array is surrounded on all sides by at least half an array, and the total area of the aperture is four times that of the detector window. This same effect could be accomplished by making the detector area four times that of the aperture, but this is more difficult and would entail a larger background. Sources lying just outside the field of view can irradiate part of the detector but not all of it. The result is that any such sources give false images in the field of view. Diffuse radiation in this outside region contributes to the background and noise in the image.

We will follow the treatment of Fenimore and Cannon (1978) in discussing image formation with a coded aperture. The authors study a particular type of $K \approx N/2$ coded aperture called by them a uniformly redundant array. Gunson and Polychronopulos (1976) and Proctor, Skinner, and Willmore (1979) give somewhat more general discussions. The coding of a coded aperture is based upon a mathematical construction called a cyclic difference set. These sets are difficult to construct and only a few are known. A compilation of known sets is given by Baumert (1971). While not all known coded apertures are half-open ($K \approx N/2$) it appears to us that, among the sets listed by Baumert, these are the most applicable to the auroral imaging problem. Fenimore and Cannon (1978) and Proctor, Skinner, and Willmore (1979) both give procedures for generating half-open apertures. As mentioned above, we choose to follow the treatment of the former authors, but the results are applicable to either type of aperture. Figure III-6 is an example of a 31 x 33 coded aperture array generated following the Proctor, Skinner, and Willmore procedure. Transmitting elements are blank.

Consider observations of an emitting object field at infinity. The time-integrated flux from an element of this source, (i, j), is O(i, j). Then the number of counts in a detector element during the exposure is given by

Figure III-6: Example of a basic coded aperture array. The transmitting cells are blank.

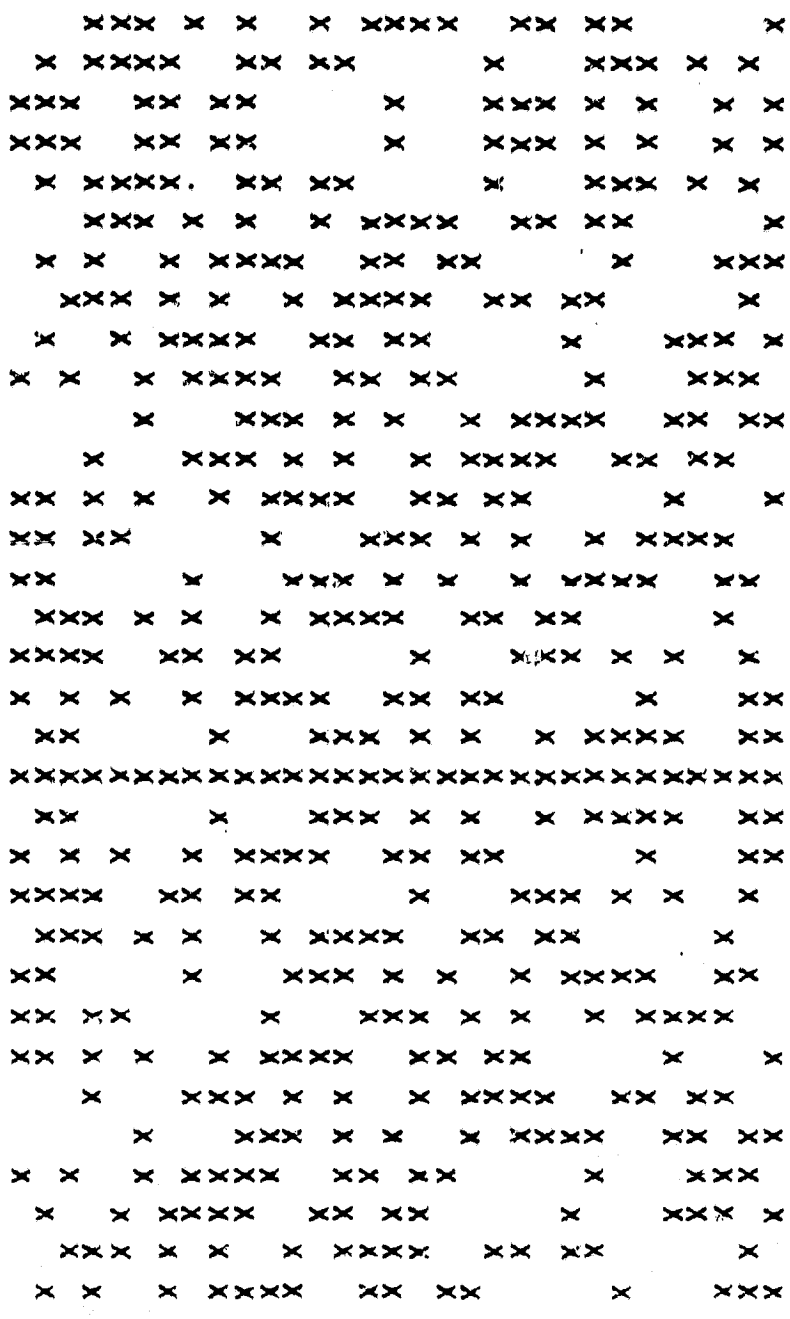

$$P(k,\ell) = \sum \varepsilon O(i,\ j)\ A(i + k,\ j + \ell) + b_{k\ell}\ , \tag{10}$$

where ε is the detector efficiency, A(m, n) is one if element (m, n) of the aperture is transmitting, and $b_{k\ell}$ is the detector background at element (k, ℓ). The array P(k, ℓ), read out by the detectors, is generally unintelligible, but the picture of the object may be obtained from it. One creates a function G(m, n) as follows:

$$\begin{gathered} G(m,\ n) = 1 \text{ if } A(m,\ n) = 1, \text{ and} \\ G(m,\ n) = -1 \text{ if } A(m,\ n) = 0. \end{gathered} \tag{11}$$

G has the property,

$$\sum_{i,j} A(i,\ j)\ G(i + k,\ j + \ell) = \frac{N + 1}{2}\ \delta_k\ \delta_\ell\ , \tag{12}$$

where $\delta_k = 1$ if $k = 0$, and $\delta_k = 0$, otherwise. There are $(N + 1)/2$ transmitting elements in a uniformly redundant array. Then the image can be reconstructed as follows:

$$I(m,\ n) = \sum_{k,\ell} P(k,\ell)\ G(k + m,\ \ell + n) =$$

$$\sum_{k,\ell} G(k + m,\ \ell + n)\ \{ \sum_{i,j} \varepsilon O(i,\ j)\ A(i + k,\ j + \ell) + b_{k\ell} \}\ . \tag{13}$$

Every element in the image is reconstructed by adding, with coefficient +1 or -1, all of the counts received by every detector element. Then the noise in

the image is simply the square root of the total number of counts recorded by the detector:

$$N(m, n) = \left[\sum_{k,\ell} P(k, \ell) \right]^{1/2} \quad \text{for all } m, n. \tag{14}$$

Now assume that the background $b_{k\ell}$ is a constant, b, independent of k,ℓ. Then since $(N+1)/2$ of the N values of G are +1 and the other $(N-1)/2$ are -1 (for a uniformly redundant array), the last sum in equation (13) is just b. Thus the expectation value of the background in each <u>image</u> element is just equal to the average background per <u>detector</u> element. Equation (13) may then be summed by reversing the summation order:

$$I(m, n) = \sum_{i,j} \varepsilon O(i, j) \sum_{k,\ell} G(k + m, \ell + n)\, A(k + i, \ell + j) + b =$$

$$\sum_{i,j} \varepsilon O(i, j)\, \delta_{im}\, \delta_{jn} + b = \varepsilon O(m, n) + b. \tag{15}$$

The expectation value of I(m, n) is $\varepsilon O(m, n) + b$ and the noise is N(m, n) given by equation (14).

For the more general arrays treated by Gunson and Polychronopulos (1976) a correlational technique is used in reconstructing the image. The result is that the object stands out above a high plateau. So that the image can be perceived more easily, the average plateau level can be subtracted out. For a half-open array, both the signal and the noise are half the corresponding values for the universally redundant array with the reconstruction technique described above. Thus, as stated earlier, the SNR is virtually the same.

We have written a computer program to simulate the performance of coded aperture systems. The program takes an arbitrary source distribution and

traces it through a coded aperture (itself generated by the program) to form the detector counting array P(k, ℓ). P(k, ℓ) is then modified by adding the background not attributable to photons passing through the mask. This added background is assumed to be independent of position. After counting statistical fluctuations are added to P(k, ℓ), the image is reconstructed by use of the technique appropriate to the type of mask. If the correlational technique is used the average height of the plateau is subtracted out before the reconstructed image is displayed.

As an example to illustrate the imaging power of a coded aperture, we have used our program to image the field in Figure III-7. The object consists of Source 2, integrated over a 10-20 keV band, alone in a 31 x 33 field covering the auroral oval. In this simulation we consider a 200-second exposure with the coded aperture system for operation in a 4 R_E orbit, to be defined below. Figure III-8 shows the leftmost columns of the detector count array, P(k, ℓ). Although wide variations are apparent, there is no discernible pattern. Finally, Figure III-9 shows the lower right hand part of the reconstructed image. The entire image is a 31 by 33 array. Since this is too large to display conveniently we show only a part of the image which contains the source. Since the reconstruction used the correlation technique, the plateau mentioned above (in this case, 24696 counts) has been subtracted from each pixel. The image stands out quite well; the measured SNR is 4.89, which is consistent with the calculated value. This demonstration shows the capability of a coded aperture to image a relatively faint object in an otherwise empty field. In practice this image would be blurred by the finite detector resolution and finite cell size in the aperture, just as pinhole camera images are blurred by the same effects.

Figure III-7: Source field for coded aperture simulation. The array of 2's is Source 2. The locations with 0's do not emit.

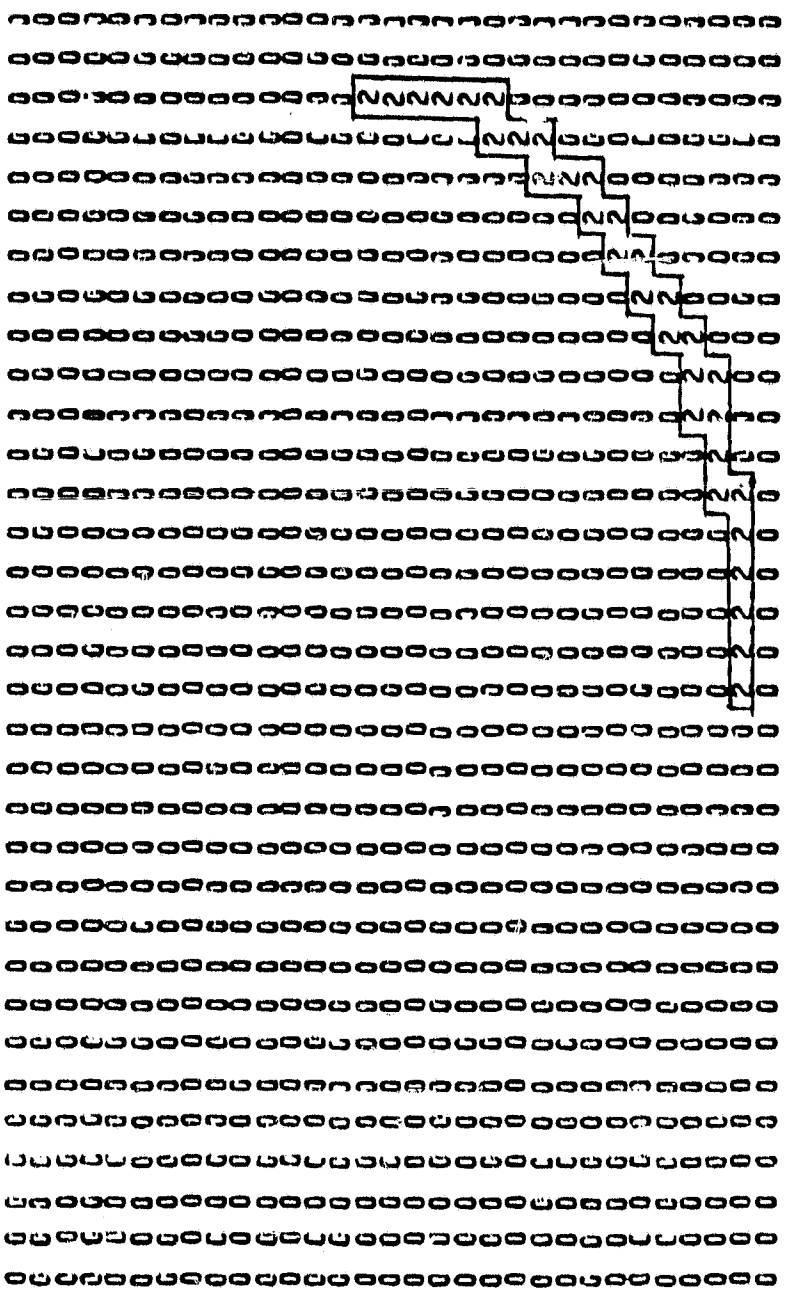

Figure III-8: The upper left hand part of the detector count array for the imaging of the source in Figure III-7. No pattern can be discerned.

Figure III-9: Part of the reconstructed image of the source in Figure III-7. A good image is obtained, with SNR = 4.89.

-74	32	207	58	56	-20	-185	-40	-118	-140	120	6	11	-27	63	124	-149	280	103	-16
20	-38	168	198	-46	218	18	8	110	103	-137	139	101	69	-44	91	-60	-237	-23	57
-194	-154	-55	-117	38	57	-61	100	108	93	20	-24	-94	113	-7	-51	-196	-2	46	120
103	-89	-70	-23	26	-27	30	-93	-97	189	104	121	-151	-147	85	-334	30	585	-32	-136
208	77	53	-1	14	-117	259	3	-154	7	-209	2	-31	102	-62	-65	-81	453	-36	60
35	-222	71	93	-96	-167	-65	-24	25	121	-79	-107	-11	-11	107	-34	-22	610	117	43
148	-18	84	53	16	-57	-266	-120	-218	89	187	171	-158	33	82	-80	71	361	-12	-17
101	-77	-117	32	-178	-34	-131	47	-201	-103	17	164	-136	9	84	-170	-66	342	-169	13
-259	-16	-80	215	102	-91	-24	70	-189	173	159	-93	-10	92	26	-8	509	464	72	6
-234	94	-66	-179	-172	-223	-2	-30	-50	-101	100	-178	-91	112	-58	121	647	30	-167	-62
11	-139	-28	35	-94	69	236	89	-163	-106	3	74	142	44	-143	413	446	-42	77	23
146	241	12	-28	-33	-84	-58	-35	136	-90	-7	-62	-103	35	97	490	-87	43	29	116
134	57	-95	-178	6	6	-147	-69	-22	-112	-121	66	124	178	514	656	-132	29	127	-2
33	193	-83	68	-92	-66	-1	-45	58	15	-84	63	-167	449	746	-53	-154	38	-86	63
-40	-205	-36	45	56	-159	-18	33	54	82	8	89	455	590	-57	229	-116	-22	26	69
-201	38	-86	-68	209	-46	-90	-152	77	155	-82	932	490	147	142	79	162	-41	40	115
-49	63	-13	-111	-60	-1	-33	-147	35	490	537	604	3	-151	6	121	-5	-20	33	-49
105	-103	154	-30	24	108	132	589	630	663	584	21	-32	186	-69	45	-101	50	91	101
158	-75	628	601	468	485	554	511	-148	-41	69	64	128	47	163	129	-42	165	-63	184
-345	-10	-35	247	0	-109	137	-2	117	-62	82	40	74	-2	-101	-107	88	-11	90	187

The coded aperture systems to be used for imaging from the various orbits are defined in a manner similar to the pinhole camera definition. However, the focal length and the desired field of view completely determine the geometry. We use a 65 cm focal length, which is about the longest usable under an overall length restriction of 75 cm. This limits the available area for a single unit, and the mass of one system is well below the 30 kg limit. To utilize the available mass more completely, we use multiple identical units. These are separately baffled and provided with separate detectors so that the solid angle does not become so large as to make the diffuse cosmic X-rays an unacceptably large noise source. The necessity for this shielding results in reduced usable area at higher orbits. Nevertheless there is some advantage in using separate systems for different orbits. This allows better observations of faint sources.

For a coded aperture, unlike a pinhole camera, the system resolution is fixed by the aperture chosen and cannot be changed in orbit. A choice of too fine resolution can result in an irreversible loss in SNR for observations of extended objects. The noise per pixel is independent of the pixel size. Suppose a faint object of large extent is being observed. One can increase the SNR by adding up four pixels in a square, effectively doubling the resolution. This increases the signal by a factor of four and the noise by a factor of two, thus doubling the SNR and quartering the detection time. In contrast, if another aperture with a doubled pixel size were used instead, the signal would be four times as large and the noise unchanged. Thus the SNR would be quadrupled and the detection time divided by 16. This illustrates the importance of making a good choice of spatial resolution. The coded apertures discussed here all have a resolution of about 0.5°. Since optimum coded apertures are known for only a few matrix dimensions (i.e., numbers of cells, N),

the angular resolution is not exactly 0.5° but varies around that value. The cell size for 0.5° resolution is substantially larger than the position sensing resolution of the detector.

The sample detection systems are designed subject to weight constraints with the same shield and detector weights per square centimeter as was the case with the pinhole camera. For 9 R_E and 15 R_E a focal length of 65 cm was used. In order to be able to use 2 systems and stay within the 30 kg mass limit the 4 R_E system was redefined to have a 60 cm focal length. Table III-4 summarizes the three systems.

Table III-4

Sample Coded Aperture Systems

Orbit (R_E)	Resolution (degrees)	(km)	Dimensions (# cells)	No. Units	Total Area (cm^2)	Ref.*
4	.57	200	31 x 33	2	733	PSW
9	.39	350	17 x 19	4	255	FC
15	.51	800	7 x 9	9	190	PSW

*FC = Fenimore and Cannon (1978)
PSW = Proctor, Skinner, and Willmore (1979)

From previous discussion in this report the SNR for a coded aperture may be written,

$$SNR = \frac{\varepsilon M_0 (K/N)\, At}{[((\varepsilon M + \varepsilon I_A\, \Omega_E + \varepsilon I_C\, \Omega_S)(K/N) + B)\, At\,]^{1/2}} , \qquad (16)$$

where, in addition to previously defined quantities,

M_0 = the flux incident on the coded aperture from the source element with which we are dealing,

A = the detector area,

t = the exposure time,

M = the flux incident on the coded aperture from the whole source,

I_A = intensity of diffuse atmospheric X-rays,

Ω_E = the effective solid angle of the Earth averaged over the detector area,

I_c = the intensity of the diffuse cosmic X-rays, and

Ω_s = the effective solid angle of the sky averaged over the detector area.

Equation (16) can be simplified as follows:

$$SNR = \frac{\epsilon M_0 \, (K/N)^{1/2} \, (At)^{1/2}}{[\epsilon M + \epsilon I_A \, \Omega_E + \epsilon I_c \, \Omega_s + (N/K) \, B]^{1/2}} \quad . \tag{17}$$

Then the time required for an SNR = 3 detection is

$$t_3 = \frac{9 \, [\epsilon M + \epsilon I_A \, \Omega_E + \epsilon I_c \, \Omega_s + (N/K) \, B]}{(\epsilon M_0)^2 \, (K/N) \, A} \quad . \tag{18}$$

We have computed t_3 for the coded aperture systems defined in Table III-4 and the four sample spectra in Figure II-6. The detector was assumed to be like that used for the pinhole camera. A numerical double integration was performed on the computer to calculate the effective solid angles, Ω_E and Ω_s. These solid angles could be reduced through the use of a collimator, but any collimator would reduce the system response at the edges of the field of view, lower the image quality, and increase the system weight. Gunson and Polychronopulos (1976) recommend that a collimator have a cell size

Table III-5

Coded Aperture SNR = 3 Detection Times

Orbit (R_E)	Source	Resolution (km)	t_3 (2-5 keV) (sec)	t_3 (10-20 keV) (sec)
4	1	200	239	3988
4	2	200	50	152
4	3	200	0.4	0.8
4	4	200	3.1	18
9	1	350	489	8.4×10^3
9	2	350	150	467
9	3	350	1.4	2.6
9	4	350	22	126
15	1	800	189	3.5×10^3
15	2	800	120	396
15	3	800	1.6	3.2
15	4	800	26	160

equal to that of the coded aperture. However, because the aurora is spatially widespread, a reduction in response at the edges of the field of view is undesirable. Besides, for the coded apertures considered here, the dominant noise contributor is rarely the diffuse X-ray spectrum. Therefore we have included no collimator. In the calculations of t_3 we have assumed that the weak widespread emission of Source 1 is always present. For the coded aperture it contributes noise to the picture (i.e., it contributes to M in equations 16-18). The detection times are tabulated in Table III-5.

The strength of the coded aperture is well illustrated in Table III-5. It lies in imaging bright compact objects in an uncrowded field. In imaging the weakest source, Source 1, the coded aperture is usually inferior to the pinhole camera. Even at 4 R_E, where the coded aperture appears to have an advantage, the 10-20 keV detection time for the pinhole camera can be reduced to an acceptable 359 s if the spatial resolution is doubled. The same sacrifice in spatial resolution for the coded aperture, made by summing four pixels in a square, improves the SNR by a factor of 2 and the detection time by a factor of 4 to 997 s. For the low background imaging considered in Table III-5 the coded aperture performance is adequate except for the case of the very faint high-energy emission of Spectrum 1.

When a bright object is in the field of view, its presence degrades the coded aperture's ability to image fainter objects. This is because M increases in equations 16-18. For example, we have repeated the simulation of the imaging of Source 2 from 4 R_E but have added an object emitting Spectrum 3, with the Source 3 solid angle, to the field of view. Again a 200 s exposure is simulated. The results are shown in Figure III-10. Only part of the image is shown. The brighter object is imaged very well, but the image quality for Spectrum 2 is poor. The SNR has decreased from 4.89 to 2.33. Table III-6

Figure III-10: Part of the reconstructed image of the source in Figure III-7 with the Source 3 added to the field. The Source 2 image is substantially degraded. Its SNR is now 2.33.

-199	52	638	128	-20	-214	-451	-77	-222	-319	235	123	139	82	145	247	-393	340	290	-347
-188	-133	197	520	84	370	-4	107	389	233	-361	320	89	-55	-9	135	-167	-443	55	201
-178	-337	-245	-347	112	-73	-231	126	287	153	-52	-2	-143	269	-13	-96	-223	-35	109	293
248	-253	-16	-192	53	-180	15	-159	-75	368	248	119	-367	-336	242	-666	166	589	-34	-247
415	191	-2	-57	-63	-238	507	24	-302	-23	-433	-75	154	123	-135	-159	-176	349	-97	134
15	-474	62	171	-215	-318	-129	-139	81	381	-81	-197	18	-20	395	-122	-72	833	176	53
333	-156	12	115	124	-229	-576	-38	-380	191	448	335	-411	89	256	-260	216	-2	-83	1
184	-119	-260	-39	-307	-89	-372	80	-387	-318	87	333	-335	-1	228	-119	-143	70	-215	153
-581	65	-73	382	300	-385	-9	249	-310	307	239	-173	-38	235	-66	0	348	362	89	134
-606	68	-72	-206	-473	-270	-73	-10	-4	-35	234	-350	-177	221	-212	274	876	122	-203	-231
79	-141	-88	57	-122	213	526	203	-411	-226	-172	265	371	138	-252	230	344	-198	186	37
272	373	-2	-59	0	-310	-239	-87	166	-102	100	-17	-334	146	187	399	-185	193	313	220
242	144	-289	-416	-37	51	-359	-123	-97	-244	-346	121	154	239	592	965	-239	58	271	184
27	11698	11141	11469	9816	26	-130	-81	81	119	-34	134	-170	455	1012	-191	-431	-16	-113	146
8998	13906	11367	11549	91	-278	-108	168	-93	182	23	91	404	746	-38	954	-144	-68	65	259
-393	38	-290	-154	373	-175	-352	-396	229	267	-82	593	642	345	305	207	455	77	83	154
-191	114	-79	-244	-197	-16	-74	-277	34	453	364	638	-5	-491	-5	25	20	-97	109	79
241	-219	302	64	1	293	156	649	714	736	640	125	-126	436	-5	149	-305	107	90	76
345	-108	655	576	346	563	743	522	-293	86	75	230	110	176	212	309	12	314	-264	466
-692	106	12	598	0	-249	276	-29	259	-175	165	112	76	-136	-105	-164	286	-137	98	309

gives the times for SNR=3 detection of Sources 1 and 2 in the presence of Source 3.

Table III-6

SNR = 3 Detection Times in the Presence of Spectrum 3

Orbit (R_E)	Source	Resolution (km)	t_3 (2-5 keV) (sec)	t_3 (10-20 keV) (sec)
4	1	200	525	1.7×10^4
4	2	200	95	428
9	1	350	1034	3×10^4
9	2	350	272	1225
15	1	800	815	2.8×10^4
15	2	800	411	2202

Table III-6 illustrates a major problem with the coded aperture. In most cases the coded aperture performance for high background imaging is worse than that of the pinhole camera. We expect the field to contain objects of a range of brightness during periods when the aurora is particularly interesting. Spectrum 2 is certainly not unusually weak. It was measured during a magnetically disturbed auroral event (Mizera et al. 1978).

The coded aperture's ability to measure bright objects, as demonstrated in Table III-5, might suggest that the observations from 9 R_E or 15 R_E be made at higher resolution. However, while auroral forms are frequently narrow in the N-S direction they are extended E-W. Thus, if the resolution is halved, the signal in a single pixel is also halved (at best) and the noise is unchanged. The latter depends only on the number of events in the detector. Thus the SNR is halved and the detection time quadrupled. This would be

unacceptable for all the sources except number 3. One could attempt to recover the sensitivity by adding together, in pairs, pixels that are adjacent in longitude. This would (again, at best) recover the original signal strength, but the noise would be increased by a factor of $\sqrt{2}$. Thus the detection time would be doubled, which is unacceptable for the weaker spectra. Therefore 0.5° resolution is about what can be achieved without a considerable sacrifice in dynamic range.

The use of a coded aperture in an eccentric orbit or in more than one orbit during a single mission has the result that the higher orbit observations have increased noise because the large solid angle required at low orbit admits more diffuse cosmic X-rays. However, under the limitations imposed for this study, the 4 R_E system has much greater active area than has the 15 R_E system. Thus if the 4 R_E system, instead of the 15 R_E system, is used at 15 R_E there is a substantial improvement in signal strength. As a result the detection times for the brighter spectra from 15 R_E are not substantially changed when the 4 R_E system is used. For spectrum 2 in the 10-20 keV band the detection time is increased from 396 s to 748 s. For spectrum 1 in the same band the increase is worse, but this radiation is, for all practical purposes, undetectable anyway. Thus there is a range of intensities for which the use of a 4 R_E aperture in a very high orbit results in a significant decrease in performance. If the field of view must be extended beyond the 60° latitude limit for imaging from 4 R_E, this degradation could be more serious.

In conclusion, the coded aperture can image bright, compact objects very well. If the experimenter is willing to sacrifice the ability to image faint objects the bright ones can be imaged with reasonably high resolution (~ 100 km from 4 R_E) on a time scale of a few minutes. In general, except for observations of very faint extended objects the coded aperture gives good perform-

ance in low orbit (~ 4 R_E). A major disadvantage of the system arises because emission anywhere in the field of view contributes to noise everywhere in the image. This results in a severe performance degradation in the simultaneous imaging of faint and bright objects. This situation is expected to arise frequently in auroral observations. A related problem is a degradation of performance from high altitudes when the orbit is eccentric. This degradation may be important only for objects in a narrow range of brightness, provided that the field of view required for low altitude observations is not too wide.

D. Rastered Collimator

In a rastered collimator observation, the collimator limits the instantaneous field of view and a mechanism rasters the pointing axis over the entire scene to be imaged. In general the performance can be expected to be no better than that of a pinhole camera of the same detector size and spatial resolution. Whereas the pinhole camera divides its area among the N source elements while observing each throughout the exposure, the rastered collimator divides its time among the source elements while observing each with the entire detector. The rastered collimator has the advantage that position sensing in the detector is unnecessary. The collimator will in many cases be less sensitive than the comparable pinhole camera, however, because it occludes part of the detector area. This effect may be offset by an increased background in the pinhole camera due to diffuse cosmic X-rays passing through "remote" pinholes. However, with the pinhole geometries and source configurations we have discussed, the diffuse background is never the dominant noise source. The pinhole camera is almost always photon limited.

The question of whether the rastered collimator is a competitive system depends upon the effective area that can be provided for a given weight. We

will consider two sorts of collimators. The first is simply an "egg crate" or "bundle of drinking straws" structure. We believe that this sort of collimator can best be constructed by using the thin aluminum hexagon cell material that is used for high strength lightweight reinforcement in the aerospace industry. The second type of collimator is the multigrid mechanical collimator discussed by McGrath (1968), Blake et al. (1976), and McKenzie, Landecker, and Underwood (1976), among others.

Consider first the hexagon cell collimator. Aluminum is a good material for a collimator of this type. It has a low atomic number so that background created by fluorescence in the collimator material is low. A very thin plastic layer on the aluminum could be applied to absorb the small number of aluminum Kα fluorescent X-rays produced. Aluminum also has sufficient X-ray absorption at glancing angles of incidence that it need not be made so thick as to cut down severely the effective detector area. Thus it is fortunate that aluminum is the standard material for hexagonal cells.

For a system comparable to the pinhole cameras and coded apertures we have considered, we set the angular resolution of the collimator at 0.5°. To be specific, if W is the distance across the hexagon from the center of one side to the center of the opposite side and L is the collimator length, then $L = W\cot(0.5°)$. With this construction, radiation off axis by 1° passes through at least one aluminum thickness, radiation 1.5° off-axis through at least two, and so forth. Thus the thickness required for adequate off-axis absorption is determined by radiation incident on the aluminum at a glancing angle of 1°. For e^{-3} transmission at 60 keV (the same criterion as used for the other systems) the requirement is that the aluminum be 0.0176 cm thick. This is nearly .007", and we will assume a .007" (7 mil) aluminum material will be used. Hexagon cell material is made in, among others, a standard 3/16" (.476 cm) cell. With this cell L = 54.6 cm and the on-axis transmission is 0.91.

The useful area can now be estimated. The cell mass per unit detector area (L = 54.6 cm) is 13.7 g/cm^2. The cell material must be rigidly supported and held in place, and, at least near the detector, it is desirable to have a graded Z shield. We assume that the shields discussed for the other detector systems, arranged around the collimator, will perform both of these functions. Again the detector mass is assumed to be 10 g/cm^2. Since a position sensitive detector is not required, the signal processing electronics can be simpler and the detector requires fewer amplifiers, discriminators, and so forth. Thus the total weight available for the detector and collimator is assumed to be 25 kg as compared to 24 kg for the coded aperture and 23 kg for the pinhole camera, which uses moving plates to change apertures. The weight criterion can be met with a detector of 729 cm^2 effective area. For comparison the pinhole camera detector with similar resolution had an area of 1116 cm^2. Thus the rastered collimator will have significantly lower sensitivity.

The discussion of the multigrid collimator follows that of McKenzie, Landecker, and Underwood (1976). The procedure for placing the grids is due to McGrath (1968). Figure III-11 depicts a multigrid collimator of length L, having N + 2 grids in total. The grid holes are square having a width W and are separated by bars of thickness t. The angular resolution is $\tan^{-1}(W/L) = 0.5°$, and the maximum angle free from side transmission lobes is θ_M. The on-axis transmission is $W^2/(W+t)^2$. The positions of the N intermediate grids (excluding the two end grids) satisfy the equation,

$$(L - \ell_n) = \frac{W}{W + t}(L - \ell_{n-1}) \; ; \; \ell_0 = 0. \qquad (19)$$

The maximum angle free from side bands is given by the equation,

Figure III-11: The procedure for placing grids in the McGrath multigrid collimator design. The collimator has no side transmission lobes for $\theta < \theta_M$.

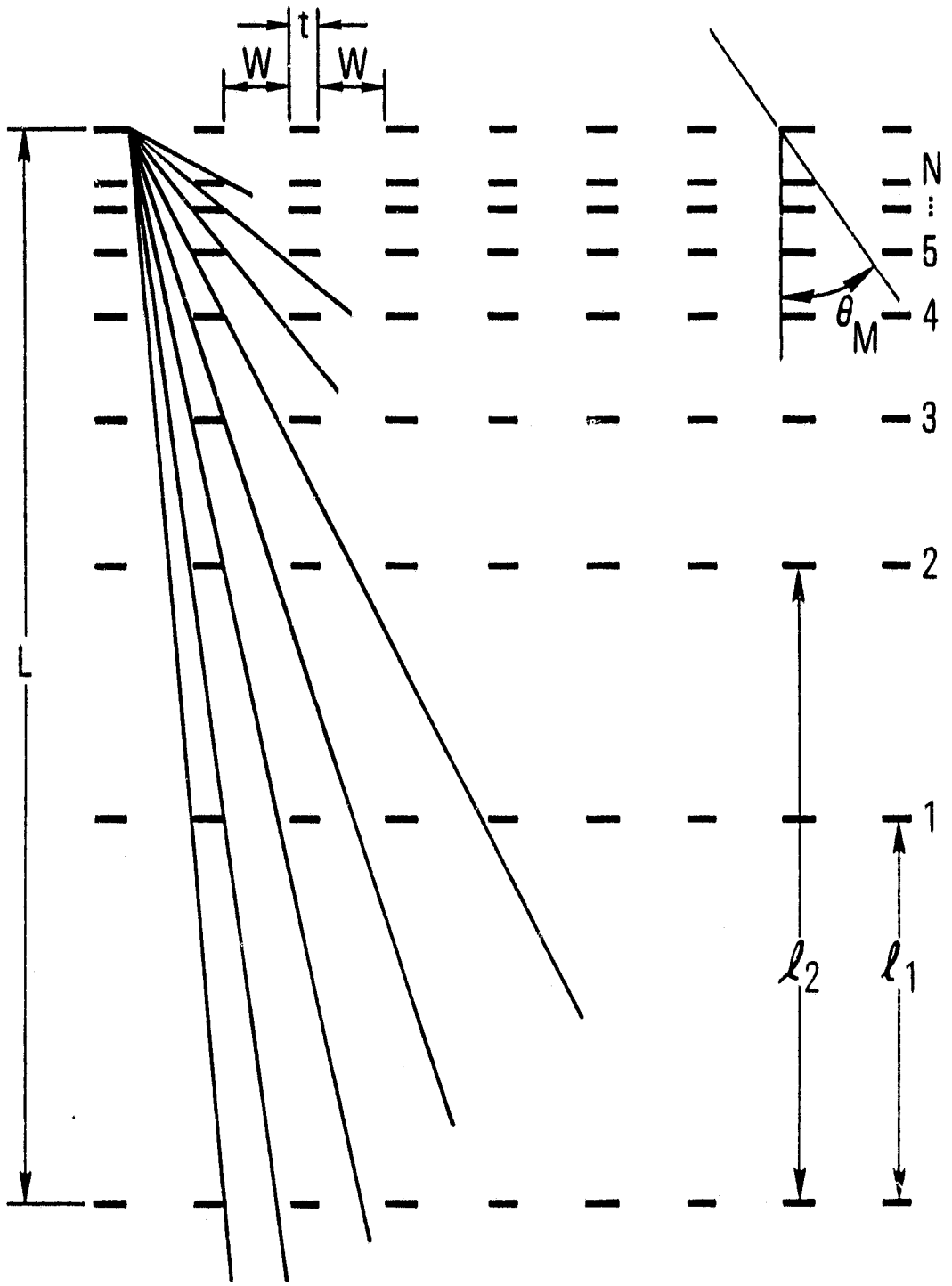
t
W
W
N
5
4
3
2
1
L
θ_M
ℓ_2
ℓ_1

$$\tan \theta_M = \frac{t}{L - \ell_N} = \left(\frac{W}{W + t}\right)^N \frac{t}{L} \quad . \tag{20}$$

This may be solved for N, where N + 2 is the total number of grids:

$$N > \frac{\log \left(\frac{L\ \theta_M}{t}\right)}{\log \left(\frac{W + t}{W}\right)} \quad . \tag{21}$$

An angular resolution of 0.5° is easy to achieve with a multigrid collimator. Astronomical experiments commonly include collimators having resolution of 1 arc minute or less (e.g., Landecker, McKenzie, and Rugge 1979). Therefore a hole-to-bar ratio of 2:1 can be used. This gives an overall transmission of ~ 0.44. Off axis rays may strike only a single grid, so each grid must absorb as well as the shielding we have considered above. We may rewrite equation (21) using the fact that the collimator resolution, ϕ, is approximately equal to W/L:

$$N > \frac{\log \left[\frac{W}{t}\ \frac{\theta_M}{\phi}\right]}{\log\ (1 + t/W)} \quad . \tag{22}$$

For an observation from a 4 R_E orbit $\theta_M = 9.1°$ if we simply require no side transmission lobes that would transmit auroral X-rays. This gives N = 9 for a total of 11 grids. The weight of the system is calculated by assuming the grids are made of the same absorbing material as the shields previously discussed, and that the collimator has similar shielding surrounding it. The objective is to maximize the effective area for a given weight. When the effective area is calculated, it is a monotonically decreasing function of L for L ≤ 65 cm. A practical limit is set by the requirement that the bars be at least as wide as the grids are thick. Since the grid thickness, for the absorbers discussed previously, is .225 cm we have

$$t = \frac{W}{2} = \frac{L \tan (0.5^0)}{2} = .225 \text{ cm} \quad . \tag{23}$$

This sets the minimum length at 51.6 cm. The resulting effective area is 435 cm^2, again significantly below that of a pinhole camera with the same weight and resolution.

The foregoing discussion shows that the rastered collimator system can be expected to be significantly less sensitive than a comparable pinhole camera. The weight of the mechanical system required to perform the rasters has not been considered. If this weight were charged to the instrument allotment the instrument sensitivity would be further reduced. The rastered collimator has the advantage that, if real time data are available, it can concentrate its observations on a small region. However for bright compact regions it is doubtful that the collimator system could improve upon the coded aperture. Our main concern here is with imaging an entire auroral zone. For this application the rastered collimator is not the best choice.

E. Imaging Collimators

An imaging collimator is a mechanical device that forms an image on a position-sensitive detector. As in the case of the rastered collimator we consider two types of collimator: a "bundle of drinking straws" and a multigrid collimator.

A collimator can be made out of a multitude of tube bundles, each of which points to a different part of the field to be imaged. The bundles must diverge from one another, so the hexagonal cell material cannot be used. Instead we consider circular tubes. The divergence has the further conse-

quence that the area (and weight) of shielding required for a given detector area and resolution is increased. Therefore we expect the area available to be less than that for a rastered collimator, and therefore less than that for a pinhole camera of the same weight and resolution. This is found to be true. When the maximum useful area is calculated for a given instrument weight, using the same assumptions as with the other instruments, it is found to be 584 cm^2 as compared to 729 cm^2 for the rastered collimator and 1116 cm^2 for the pinhole camera.

Bradt, et al. (1968) discuss an imaging multigrid collimator. However this collimator has an on-axis transmission of $(1/2)^{2K}$, where K is the number of grids. For an auroral imager useful at 4 R_E and having an angular resolution of 0.5°, K=7. Clearly this is unsatisfactory.

A better multigrid collimator, described by Van Beek (1976) is illustrated in Figure III-12. The collimator is broken up into subcollimators, each of which looks in a specific direction. The hole size, W, and the bar size, t, are both constants for every grid and for every subcollimator. If the spatial resolution, and the separation between view directions for adjacent subcollimators is ϕ, then $d_f = d_b + L\tan\phi$, where the symbols are defined in the figure. In order to obtain a field of view of $\pm \theta_M$ the plates must get progressively larger so that the front plate has a width equal to the width of the back plate plus $2L\tan\theta_M$. This results in a use of weight that is inefficient, even when compared to a nonimaging multigrid collimator. We have calculated the effective area for a W/t = 2 imaging multigrid collimator with resolution 0.5° and $d_b = t$. The collimator grids, eleven in all, were located according to the discussion accompanying Figure III-11. This allowed the weight of each grid to be calculated. Assumptions regarding the grid weights, the shields, and the detector were the same as those for the rastered multi-

Figure III-12: The sub-collimator type of imaging multigrid collimator.

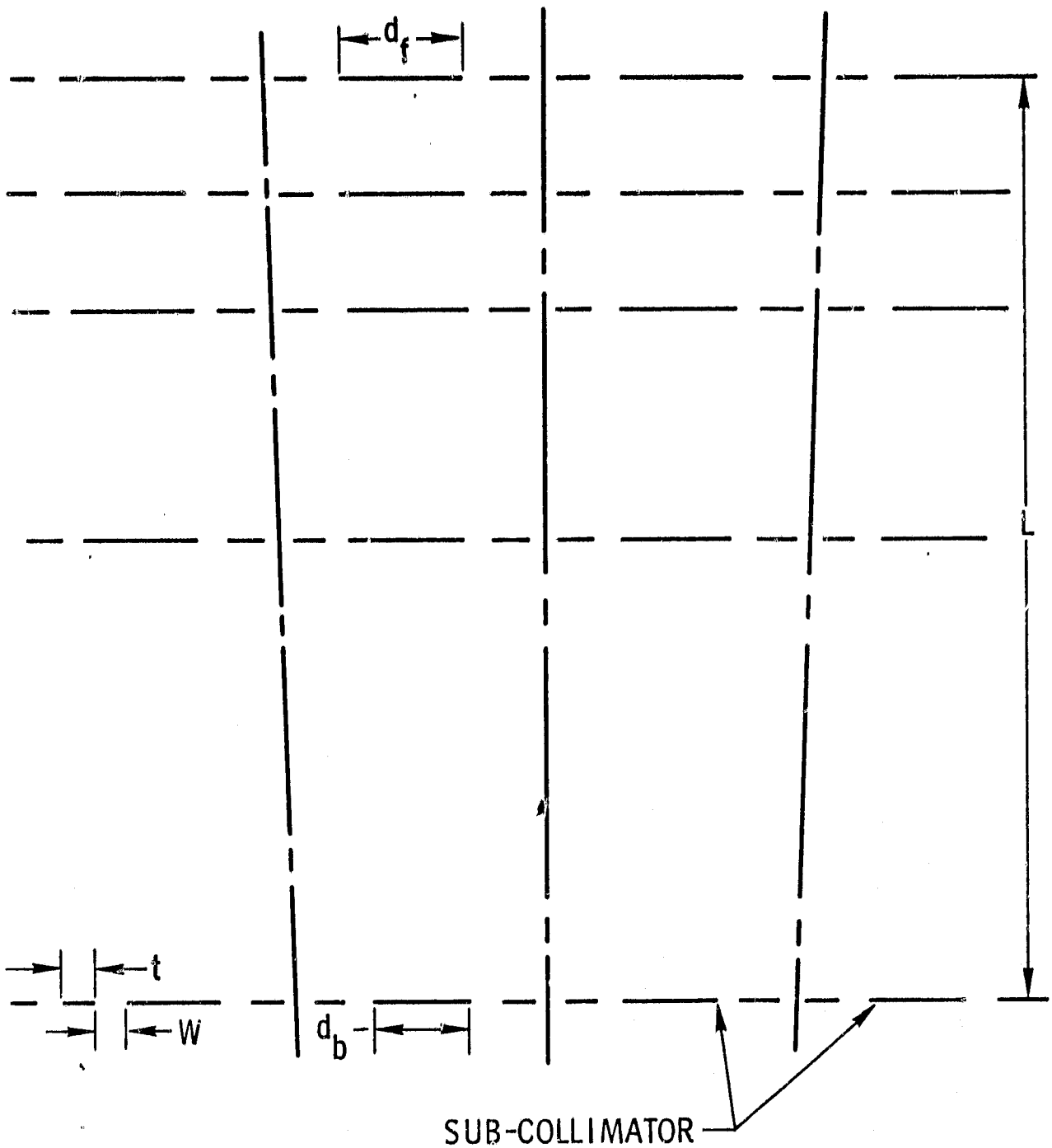
d_f
L
t
W
d_b
SUB-COLLIMATOR

grid collimator. As in that case, the minimum length L was set at 51.6 cm by the requirement that t be at least as large as the grids are thick. The optimum system's useful area was found to be 369 cm^2.

Fenimore and Blake (1980) describe multigrid collimators with random hole patterns. The chief advantage of these systems is that the "pile up" of grids at one end of the collimator that is characteristic of the McGrath (1968) design is avoided; the grids are equally spaced. On-axis transmission approaching that of the McGrath collimator can be achieved. Unfortunately, beyond a certain distance off axis, the collimator has a small transmission. This poses a problem for observing extended auroral sources, which may be quite bright far away from the center of the field of view. An imaging collimator can be made using the random pinhole grids, but its transmission on axis will be no better than that of the multigrid imaging collimator discussed above. Furthermore the small degree of off-axis leakage can be important. Therefore the random hole collimator is unsuitable for auroral observations.

In summary, the imaging collimator is much like a pinhole camera but has significantly less effective area. It has two advantages that might partially compensate for the smaller signal. First, all of the parts of the detector viewing the same source element can be in the same place. With the multiple pinhole camera the parts of the detector looking in the same direction are regions the size of the pinholes distributed all over the detector. A similar situation prevails for the coded aperture. Thus the position sensing ability of the detector used with the latter two systems needs to be better than that of an imaging collimator's detector. However the signal strength imposes a limit on the resolution of all three systems that is more severe than that imposed by current position-sensitive detector technology. The second advantage over the pinhole camera is the lower diffuse X-ray background already

mentioned in the discussion of rastering collimators. As we pointed out earlier, this advantage does not compensate for the loss of area.

IV. DISCUSSION

Five types of candidate auroral X-ray imaging systems were discussed in Section III. The two types of collimated detectors were found to have significantly poorer performance than the pinhole camera and the coded aperture. They are therefore judged unsuitable for use in global (or "semi-global") auroral X-ray imaging. In addition, the X-ray telescope lacks the ability to extract the spectral information needed in reconstructing the electron spectrum. This reconstruction is a necessary first step in deriving useful geophysical information from the X-ray images. Hence the X-ray telescope is judged to be an incomplete solution to the problem under discussion. On the other hand, in almost all situations, the X-ray telescope provides higher image quality than the other systems do. On this account, and because it could be used in conjunction with another X-ray imager, we will not eliminate the telescope from consideration. Therefore, in this section we discuss the suitability of the pinhole camera, coded aperture, and X-ray telescope under various observing conditions. We consider orbital configurations and spacecraft accommodations. At the end of the section we summarize the conclusions of the study.

A. Orbit

Figure IV-1 illustrates elliptical (on the left) and circular high altitude orbits. The elliptical orbits have their apogees over the north magnetic pole. The elliptical orbits have apogees of n x R_E, where n is an integer, and perigees of 7000 km, both measured from the center of the Earth. Each orbit is labeled by its apogee in units of R_E. The available observing times, discussed below, are not very sensitive to perigee. For example, increasing

Figure IV-1: Elliptical and circular orbits for high altitude remote sensing of the aurora. The polar cap is completely visible when the satellite is above the H lines. Radiation belt electron flux contours are also shown.

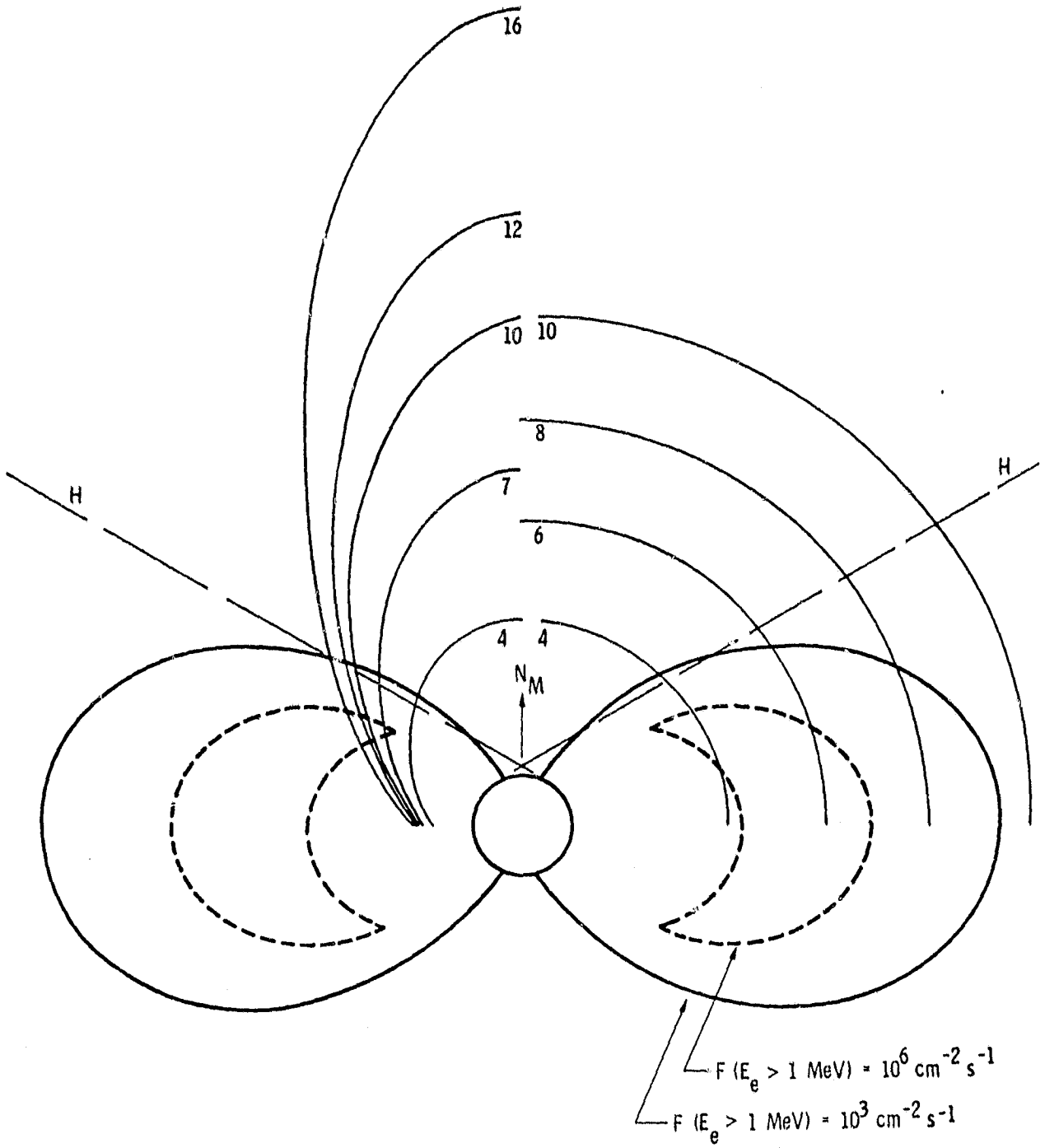
16
12
10
10
8
7
6
4
4
H
H
N_M
F (E_e > 1 MeV) = 10^6 cm^{-2} s^{-1}
F (E_e > 1 MeV) = 10^3 cm^{-2} s^{-1}

the perigee to 8000 km increases the length of time available to observe a single polar region during each orbit, but reduces the percentage of time that one polar region is visible by around 2%. Therefore, in terms of observing periods, the elliptical orbits discussed below are representative of the high altitude eccentric polar orbits that would be used for an auroral imaging program.

We have used Figure IV-1 to determine the time intervals during which an experiment could view an entire polar region for various orbits. The polar region is assumed to be that region lying within 30° of the magnetic pole. In the figure the dashed lines labeled H are the limits below which the north polar region is not entirely visible. This places one limit on the viewing time. The figure also includes electron flux contours. Both the pinhole camera and the coded aperture use large area detectors that are sensitive to electrons. High electron fluxes give rise to a background that can make imaging impossible. The problem is especially acute with the coded aperture since it has a large open area and solid angle. The pinhole camera has both a small open area and a small solid angle. Furthermore, small "broom magnets" can be positioned around the few pinholes that are open at low altitude so that electrons passing through the pinholes are deflected away from the detector. Then the pinhole camera will be disturbed only by electrons having sufficient energy to penetrate the shielding (~ 3 MeV at normal incidence). The coded aperture may be disabled by background electron fluxes even above the H lines in Figure IV-1.

For circular orbits each polar region is observable for something less than one-third of each orbit. For more than one-third of the time neither polar region is completely visible. The long period during which the experiment is out of touch with a given polar cap is a major disadvantage of high

circular orbits. A satellite in a 15 R_E circular orbit spends almost 2.3 consecutive days during which it cannot image the entire north polar region and more than 13.6 consecutive hours during which neither polar region can be entirely imaged. An X-ray telescope, with its small field of view, would gain some advantage from a high circular orbit ($\sim$15 R_E apogee) since the time during which it could simultaneously image the whole polar region would be relatively long. However, even for the telescope, the high circular orbit may not be the best choice.

The properties of the elliptical orbits are summarized in Table IV-1. Again, all orbits have a 7000 km perigee. The parameter r_H is the distance of the satellite from the center of the Earth when the satellite crosses the H lines in Figure IV-1. The observing interval is the time during which the satellite is above the H lines. For the coded aperture the observing interval may be shorter because of electrons in the radiation belts. It is desirable that the observing interval be at least four hours because this is the duration of a complete magnetic substorm. This means that the apogee should be around 5 R_E or higher. Two other factors make a high apogee desirable. First, the percentage of time available for imaging a complete polar cap increases with height. Second, r_H also increases with apogee. Increasing r_H decreases the field of view that is required. This may permit more pinholes without overlapping images in the pinhole camera and a smaller diffuse cosmic X-ray background for the coded aperture. On the other hand, the coded aperture and pinhole camera both have better spatial resolution (in km) when they are nearer the source being imaged. Therefore, for these systems, an apogee somewhat higher than 5 R_E would be best. The X-ray telescope has good spatial resolution at all the altitudes under consideration, so a high apogee orbit is most desirable. The difference between the orbital period and the observing

Table IV-1
Observation Times for Elliptical Orbits

Apogee (R_E)	Period (sec)	r_H (R_E)	Observing Interval (sec)	(percent)
4	2.06×10^4	3.0	1.16×10^4	56.1
6	3.38×10^4	3.7	2.39×10^4	70.6
8	4.91×10^4	4.1	3.84×10^4	78.3
10	6.61×10^4	4.4	5.48×10^4	82.9
12	8.48×10^4	4.6	7.33×10^4	86.4
14	1.05×10^5	4.8	9.30×10^4	88.7
16	1.26×10^5	4.9	1.14×10^5	90.5
18	1.49×10^5	5.0	1.37×10^5	91.8
20	1.73×10^5	5.1	1.61×10^5	92.9

interval is the time interval during which the entire polar cap cannot be imaged. Even for the highest elliptical orbits this period is less than 3.5 hours.

The Polar Plasma Laboratory (PPL) satellite, part of NASA's planned Origins of Plasmas in the Earth's Neighborhood (OPEN) program is a potential platform for an auroral X-ray imaging experiment. The satellite will spend the first 18 months of its mission in a 15 R_E apogee orbit and then will be placed in a 4 R_E apogee orbit. From Table IV-1, one can expect to be able to make observations from distances as small as about 3 R_E and as large as 15 R_E during the mission. A large range of fields of view is required, and this favors the flexibility of the multiple pinhole camera. With a large field of view the coded aperture's ability to detect faint sources from the higher altitude orbit is reduced because of image noise arising from diffuse cosmic X-rays. The X-ray telescope would provide good images from the PPL orbits, but no information on the precipitating electron spectra.

B. Satellite Accommodations

To allow the best possible X-ray images and spectra of the aurora to be obtained, the satellite should provide a pointing platform for the imager. X-ray images can be made from a spinning satellite that sweeps the imager field of view across the polar cap to be imaged, but the sensitivity of the measurement depends upon the duty cycle that can be obtained. The multiple pinhole camera can obtain a duty cycle of ten percent or more if the pinholes are fanned out along the direction of rotation. The duty cycle is limited by the uncertainty in the photon location (on the detector window) that arises from the uncertainty in the interaction depth (in the detector) of obliquely incident photons. This uncertainty can be reduced by decreasing the wire layer

spacing in the detector, but a "drift length" of a centimeter or more, between layers, is needed to maximize the position location resolution. The coded aperture cannot have such a large duty cycle because the solid angle would become so large that diffuse cosmic X-ray noise would degrade the image. Furthermore, while the pinhole camera or X-ray telescope event source can be precisely located in space if the instrument aspect is known as a function of time, coded aperture events cannot be so easily "despun" because events in a given detector location can come from a wide range of directions. Reconstruction of the image then becomes a complex process. The duty cycle for the X-ray telescope is the field of view divided by 360° for a source that is swept over by the viewing axis. Off axis sources have smaller duty cycles. Therefore the X-ray telescope duty cycle would be about 10^{-2} or less. For a spinning platform only the pinhole camera is suitable. The spatial resolution or sensitivity would have to be significantly degraded from the performance discussed in Section III, but useful and worthwhile results could be obtained.

The small field of view of the X-ray telescope imposes demands on the satellite pointing system. Unless the satellite is in a very high (~ 15 R_E) circular orbit, a number of pointings will be required in making an image . For example, we found earlier that when the satellite is at 4 R_E the telescope must be pointed 16 times in 300 seconds to build up an image. This would require either a complex preprogrammed pointing sequence or a great deal of real-time commanding. Furthermore, the programming requirement would impose a preselected exposure time on the observations. With the other systems the experimenter could select ex post facto an interval of data of arbitrary length and call the selected interval an exposure. Thus a short dynamic event could be analyzed separately. Finally, only near apogee would the telescope be able to image the whole field simultaneously. These considerations might

lead one to choose a high altitude circular orbit for an X-ray telescope. This has the disadvantages of coverage we discussed above.

It is likely that an auroral X-ray imaging experiment will first be flown on a satellite whose design and orbit are dictated by the need to accommodate a variety of experiments. Imaging of the aurora in X-rays may be only a minor design consideration. The OPEN PPL is such a satellite. The satellite will operate in two orbits, neither of which is ideal for X-ray imaging. Furthermore, it is not clear that the satellite will have the pointing capabilities needed to allow optimum imaging in the X-ray region. The satellite will probably have a despun, orientable platform that will provide pointing with adequate accuracy to meet the needs of an X-ray imager. However the satellite will carry a variety of particles and fields and imaging experiments which will have pointing requirements of their own which are different from those of the X-ray imager. It is therefore unlikely that the X-ray imager will have the pointing control it needs for optimum observations. Time sharing of the pointer will at least be required. In fact it may not be possible to accommodate the imager on the pointed platform at all. In the event that the imager had to be mounted on the spinning body of the satellite, the pinhole camera would be the only suitable system. If pointing is provided, either the pinhole camera or the coded aperture can fulfill the imaging objectives, but the former instrument is more adaptable to the wide variations in the field of view that result from the operations in both high and low apogee eccentric orbits.

C. Summary and Conclusions

The study summarized in this report was an examination of the feasibility of imaging the aurora in X-rays from a high altitude satellite, using various

instrumental techniques. The objective was to specify one or more instrumental systems capable of doing the imaging. In addition we sought to specify optimum orbit configurations and satellite accommodations for each feasible technique.

The first step in the study was to define the problem. The desirability of auroral imaging in the X-ray region arises from two main factors. First the aurora can be imaged in X-rays at all local times, day and night. Provided that the observations are restricted to an energy above about 2 keV, daytime auroral imaging is possible even during periods of unusually high solar activity. The second advantage is that measurement of the X-ray spectrum allows the recovery of the electron spectrum in a straightforward manner. The feasibility of this process has been demonstrated by work with the Aerospace DMSP F2 X-ray sensor data. It is desirable to make spectral measurements at as high an energy as is permitted by the available flux, so that the electron spectrum can be described as completely as possible.

Knowledge of the auroral X-ray spectra and the background spectra is essential to the study. The DMSP F2 data showed that a wide variety of auroral X-ray spectra and morphologies exist. Four representative sources were selected as examples to be used in evaluating the proposed imaging techniques. Background arises from diffuse cosmic and atmospheric X-rays, and from the interactions of solar X-rays in the sunlit Earth's atmosphere. The diffuse cosmic X-ray spectrum is well known in the 2-100 keV band (Schwartz and Gursky 1974). The atmospheric X-ray spectrum is based on an extrapolation to low energies of high latitude measurements by Imhof, Nakano, and Reagan (1976). Using data from the Aerospace X-ray spectrometer/spectroheliograph on the P78-1 satellite, we obtained an estimate of the solar X-ray albedo spectrum at a time of high solar activity. Previous measurements with the HEAO A-

l experiment (Rugge, McKenzie and Charles 1979) found a much weaker spectrum at a quieter time.

The major part of the study was an evaluation of five candidate imaging systems: X-ray telescope, multiple pinhole camera, coded aperture, rastered collimator, and imaging collimator. The advantages and disadvantages of each system are summarized in Table IV-2. The X-ray telescope was found to be capable of producing high resolution images, but its energy range is restricted to below about 4 keV. This is inadequate for the derivation of the electron spectrum and the geophysical information that follows from it. Therefore an X-ray telescope is judged to be an incomplete experiment. The two collimated experiments were found to be significantly less sensitive than the pinhole camera and coded aperture and were therefore eliminated from further consideration.

The choice between the pinhole camera and coded aperture as the optimum imaging instrument depends upon a number of considerations. The coded aperture has a decided advantage in imaging compact, bright sources, but its performance in measuring weak spectra degrades in the presence of strong emitters. The coded aperture sensitivity is diminished for observations near apogee in high, elliptical orbits because the wide field of view required for low altitude imaging results in increased image noise from diffuse cosmic X-rays at high altitudes. The coded aperture appears to be the best choice for obsevations from low altitude (~ 4 R_E), while the flexibility provided by variable pinhole configurations favors the pinhole camera for high elliptical orbits or satellites which fly in both high and low apogee elliptical orbits during their missions. If pointing cannot be provided, but the experiment is aboard a spinning satellite that sweeps the field of view across the polar cap, the pinhole camera is the best choice. The optimum orbit for either

Table IV-2

Auroral X-Ray Imaging Techniques

System	Advantages	Disadvantages
X-Ray Telescope	1. Excellent spatial resolution.	1. Energy range limited to 4 keV. 2. Multiple pointings required except in high circular orbit for which duty cycle is relatively small.
Multiple Pinhole Camera	1. Variable FOV and spatial resolution. 2. Adaptable to spinning satellite.	1. Limited spatial resolution.
Coded Aperture	1. High sensitivity for faint background imaging.	1. Low sensitivity for weak sources in the presence of bright ones. 2. Susceptible to charged particle background.
Rastered Collimator	1. Does not need position sensitive detector.	1. Low sensitivity. 2. Requires rastering mechanism.
Imaging Collimator	1. Position sensing detector requirements relatively mild.	1. Low sensitivity.

C-2

instrument appears to be a moderate altitude ($\gtrsim 5$ R_E) elliptical one. This permits continuous observation of entire substorms. The apogee selection depends on a trade-off between spatial resolution and percentage of time coverage. The pinhole camera and coded aperture are both expected to perform well in this type of orbit.

In conclusion, we have found that auroral X-ray imaging is feasible and capable of producing physically useful results that are not otherwise available. Two imaging systems, the multiple pinhole camera with variable pinhole configurations and the coded aperture, are best able to provide the needed global images and spectra. The choice between the two depends upon the orbit and satellite accommodations. Either system works well in an optimum elliptical orbit having an apogee over a polar cap at an altitude of around 5 R_E or slightly higher.

REFERENCES

Blake, R. L., Santos, P. F., Barrus, D. M., Brubaker, W., Fenimore, E., and Puetter, R. 1976, Space Sci. Inst., 2, 171.

Baumert, L. D. 1971, "Cyclic Difference Sets," Lecture Notes in Mathematics #182, (Springer-Verlag), p 150.

Bradt, H., Garmire, G., Oda, M., Spada, G., Sreekantan, B. V., Gorenstein, P., and Gursky, H. 1968, Space Sci. Rev., 8, 471.

Catura, R. C. and Smithson, R. C. 1979, Rev. Sci. Inst., 50, 219.

Davis, T. Neil 1978, Space Sci. Rev., 22, 77.

Fenimore, E. E. and Blake, R. L. 1980, Rev. Sci. Inst., 51, 445.

Fenimore, E. E. and Cannon, T. M. 1978, Applied Optics, 17, 337.

Gunson, J. and Polychronopulos, B. 1976 Mon. Not. R. Astr. Soc., 177, 485.

Gursky, Herbert and Schwartz, Daniel, X-ray Astronomy, ed. R. Giacconi and H. Gursky (Dordrecht: D. Reidel), p. 73.

Imhof, W. L. 1974, Int. Conf. on X-rays in Space (Calgary: Univ. of Calgary), p 741.

Imhof, W. L., Nakano, G. H., and Reagan, J. B. 1976, J. G. R., 81, 2835.

Landecker, P. B., McKenzie, D. L., and Rugge, H. R. 1979, Proc. S. P. I. E., 184, 285.

Long, K. S., Reid, P. B., Ku, W. H.-M., Mitchell, D. D., Novick, R., and Pisarski, R. L. 1979, Proc. S. P. I. E. 184,, 239.

Luhmann, J. G. and Blake, J. B. 1977, J. Atmos. Terr. Phys., 39, 913.

Mangus, J. D. and Underwood, J. H. 1969, Applied Optics, 8, 95.

McGrath, John F., Jr. 1968, Rev. Sci. Inst., 39, 1036.

McKenzie, D. L., Landecker, P. B., and Underwood, J. H. 1976, Space Sci. Inst., 2, 125.

Mizera, P. F., Luhmann, J. G., Kolasinski, W. A., and Blake, J. B. 1978, J. G. R., 83, 5573.

Pal, Y. 1973, X- and Gamma-Ray Astronomy, I. A. U. Symp. #55, 279.

Proctor, R. J., Skinner, G. K., and Willmore, A. P. 1978, Mon. Not. R. Astr. Soc., 187, 633.

Rothschild, R., Boldt, E., Holt, S., Serlemitsos, P., Garmire, G., Agrawal, P., Riegler, G., Bowyer, S., and Lampton, M. 1979, Space Sci. Inst., 4, 269.

Rugge, H. R., McKenzie, D. L., and Charles, P. A. 1979, Space Res., XIX, 243.

Schwartz, D. A., Griffiths, R. E., Murray, S. S., and Zombeck, M. V. 1979, Proc. S. P. I. E., 184, 247.

Schwartz, Daniel and Gursky, Herbert 1974, X-ray Astronomy, ed. R. Giacconi and H. Gursky (Dordrecht: D. Reidel), p. 366.

Vaiana, G. S. 1978, New Instrumentation for Space Astronomy: COSPAR Advances in Space Exploration 1, ed. K. A. Van Der Hucht and G. Vaiana (Oxford: Pergamon Press), p. 177.

Van Beek, H. F. 1976, Space Sci. Inst., 2, 197.

Van Speybroeck, Leon P. 1979, Proc. S. P. I. E., 184, 2.

Wolter, Hans 1952, Annalen der Physik 6. Folge, 10, 94.